AIRBORNE CMUT CELL DESIGN

A DISSERTATION SUBMITTED TO
THE DEPARTMENT OF ELECTRICAL AND ELECTRONICS ENGINEERING
AND THE GRADUATE SCHOOL OF ENGINEERING AND SCIENCE
OF BILKENT UNIVERSITY
IN PARTIAL FULFILLMENT OF THE REQUIREMENTS
FOR THE DEGREE OF
DOCTOR OF PHILOSOPHY

By
Aslı Yılmaz
July, 2014

In reference to IEEE copyrighted material which is used with permission in this thesis, the IEEE does not endorse any of Bilkent University's products or services. Internal or personal use of this material is permitted. If interested in reprinting/republishing IEEE copyrighted material for advertising or promotional purposes or for creating new collective works for resale or redistribution, please go to http://www.ieee.org/publications_standards/publications/rights/rights_link.html to learn how to obtain a License from RightsLink.

I certify that I have read this thesis and that in my opinion it is fully adequate, in scope and in quality, as a dissertation for the degree of Doctor of Philosophy.

Prof. Dr. Hayrettin Köymen(Advisor)

I certify that I have read this thesis and that in my opinion it is fully adequate, in scope and in quality, as a dissertation for the degree of Doctor of Philosophy.

Prof. Dr. Abdullah Atalar(Co-Advisor)

I certify that I have read this thesis and that in my opinion it is fully adequate, in scope and in quality, as a dissertation for the degree of Doctor of Philosophy.

Prof. Dr. Yusuf Ziya İder

I certify that I have read this thesis and that in my opinion it is fully adequate, in scope and in quality, as a dissertation for the degree of Doctor of Philosophy.

Asst. Prof. Mehmet Z. Baykara

I certify that I have read this thesis and that in my opinion it is fully adequate, in scope and in quality, as a dissertation for the degree of Doctor of Philosophy.

Asst. Prof. Dr. Arif Sanlı Ergün

I certify that I have read this thesis and that in my opinion it is fully adequate, in scope and in quality, as a dissertation for the degree of Doctor of Philosophy.

Asst. Prof. Dr. Barış Bayram

Approved for the Graduate School of Engineering and Science:

Prof. Dr. Levent Onural
Director of the Graduate School

Copyright Information

©2014 IEEE. Reprinted, with permission, from A. Unlugedik, A. S. Tasdelen, A. Atalar, H. Koymen, "Designing Transmitting CMUT Cells for Airborne Applications" , IEEE Transactions on Ultrasonics, Ferroelectrics, and Frequency Control, accepted to publish.

©2013 IEEE. Reprinted, with permission, from A. Unlugedik, A. Atalar, H. Koymen, "Designing an efficient wide bandwidth single cell CMUT for airborne applications using nonlinear effects" , IEEE International Ultrasonics Symposium, July 2013.

©2012 IEEE. Reprinted, with permission, from A. Unlugedik, A. Atalar, C. Kocabas, H. K. Oguz, H. Koymen, "Electrically Unbiased Driven Airborne Capacitive Micromachined Ultrasonic Transducer Design" , IEEE International Ultrasonics Symposium, October 2012.

ABSTRACT

AIRBORNE CMUT CELL DESIGN

Aslı Yılmaz
Ph.D. in Electrical and Electronics Engineering
Advisor: Prof. Dr. Hayrettin Köymen
Co-Advisor: Prof. Dr. Abdullah Atalar
July, 2014

All transducers used in airborne ultrasonic applications, including capacitive micromachined ultrasonic transducers (CMUTs), incorporate loss mechanisms to have reasonably wide frequency bandwidth. However, CMUTs can yield high efficiency in airborne applications and unlike other technologies, they offer wider bandwidth due to their low characteristic impedance, even for efficient designs. Despite these advantages, achieving the full potential is challenging due to the lack of a systematic method to design a wide bandwidth CMUTs. In this thesis, we present a method for airborne CMUT design. We use a lumped element circuit model and harmonic balance (HB) approach to optimize CMUTs for maximum transmitted power.

Airborne CMUTs have narrowband characteristic at their mechanical part, due to low radiation impedance. In this work, we restrict the analysis to a single frequency and the transducer is driven by a sinusoidal voltage with half of the frequency of operation frequency, without any dc bias. We propose a new mode of airborne operation for CMUTs, where the plate motion spans the entire gap. We achieve this maximum swing at a specific frequency applying the lowest drive voltage and we call this mode of operation as Minimum Voltage Drive Mode (MVDM).

We present equivalent circuit-based design fundamentals for airborne CMUT cells and verify the design targets by fabricated CMUTs. The performance limits for silicon membranes for airborne applications are derived. We experimentally obtain 78.9 dB//20Pa@1m source level at 73.7 kHz, with a CMUT cell of radius 2.05 mm driven by 71 V sinusoidal drive voltage at half the frequency. The measured quality factor is 120.

CMUTs can achieve a large bandwidth (low quality factor level) as they can

be manufactured to have thin plates. Low-quality-factor airborne CMUTs experience increased ambient pressure and therefore a larger membrane deflection. This effect increases the stiffness of the plate material and can be considered by nonlinear compliance in the circuit model. We study the interaction of the compliance nonlinearity and nonlinearity of transduction force and show that transduction overwhelms the compliance nonlinearity.

To match the simulation results with the admittance measurements we implement a very accurate model-based characterization approach where we modify the equivalent circuit model. In the modified circuit model, we introduced new elements to include loss mechanisms. Also, we changed the dimension parameters used in the simulation to compensate the difference in the resonance frequency and amplitude.

Keywords: Airborne Capacitive Micromachined Ultrasonic Transducers, Circular CMUT, MEMS, Lumped Element Model, Equivalent Circuit Model, Unbiased Operation, High Efficiency.

ÖZET

HAVADA ÇALIŞAN CMUT HÜCRELERİ

Aslı Yılmaz
Elektrik Elektronik Mühendisliği, Doktora
Tez Danışmanı: Prof. Dr. Hayrettin Köymen
Tez Eş Danışmanı: Prof. Dr. Abdullah Atalar
Temmuz, 2014

Kapasitif mikroişlenmiş ultrasonik çeviriciler (CMUT) de dahil havada ultrasonik çalışmalar için kullanılan bütün çeviriciler frekansta geniş bant elde etmek için kayıp mekanizması kullanmaktadırlar. CMUT'lar havadaki uygulamalarında diğer teknolojilerden farklı olarak yüksek verim gösterirler, düşük karakteristik empedansa sahip oldukları için verimli tasarımlarda da geniş bantlı çalışma özelliğine sahiptirler. Geniş bantlı CMUT tasarımı için sistematik bir metot olmadığından bahsedilen bu avantajlarından tam olarak faydalanılamamaktadır. Bu çalışmada, havada çalışan CMUT dizaynı için bir metot anlatılmaktadır. Toplu eleman devre modeli ve harmonik dengeleme (HB) yaklaşımı uygulanmıştır. Bu metot CMUT'lardan maksimum güç elde etmek için optimize edilmiştir.

Havada çalışan CMUT'lar düşük radyasyon empedansı sebebi ile mekanik kısımda dar bantlı karakteristiğe sahiptirler. Bu çalışma tek tonda frekans analizleri için kısıtlanmıştır. Elektriksel taraftan giriş sinyali olarak doğru akım (DA) olmadan frekansı çalışma frekansının yarısında sinüsoidal sinyal kullandık. Havada çalışan CMUT'lar için üst plakanın bütün hareket alanını (CMUT boşluğunun tamamını) kullanan yeni bir mod tanımladık. Bu maximum genlik hareketine özel bir frekansta en kücük voltaj genligi ile ulaştık ve bu yeni moda Minimum Voltajda Sürme Modu (MVDM) adını verdik.

Denkleştirilmiş devre modeli kullanarak havada çalışan CMUT hücreleri için dizayn temellerini çalıştık ve çıkarılan dizayn hedeflerini üretilen CMUT'lar ile doğruladık. Havadaki uygulamalar için silikon kullanılmış üst plakaya sahip CMUT'ların performans sınırları incelendi. Deneysel olarak, çalışma frekansının yarısı kullanılarak çalıştırılan 2.05 mm yarıçaplı CMUT hücresinden 71 V uygulayarak 73.7 kHz'te 78.9 dB//20Pa@1m kaynak seviyesi elde ettik. Bulunan kalite faktörü 120'dir.

CMUT'larda geniş bant (düşük kalite faktörü) elde edebilmek için, üretimlerinin ince plaka ile yapılması gerekir. Düşük kalite faktörlü CMUTlar ortam basıncından çok fazla etkilenir ve böylece plaka bükülmesi fazla olur. Bu da plakanın yapıldığı malzeme sertliğinin artışına sebep olur. Bu sertlik devre modelinde kullanılan doğrusal olmayan ka–pasitans ile modellenir. Tezde, kapasitanstan kaynaklanan ve kuvvetten kaynaklanan doğrusal olmama özelliği incelenmiş, CMUT'lar için her zaman kuvvetten kaynaklanan doğrusal olmama özelliğinin baskın olduğu gösterilmiştir.

Tam doğru çalışan bir model tabanlı karakterizasyon yöntemi admitans ölçümlerinin benzeşim sonuçlarıyla tutarlılık göstermesi için kullanılmış eşdeger devre bu uyuşmanın olacagı şekilde modifiye edilmiştir. Modifiye edilen modelde yeni elemanlar gercekte kayıpları modellemek için kullanılmıştır. Ayrıca modelde kullanılan parametreler rezonans frekansının yerini ve genliğini bulabilmek için değiştirilmiştir.

Anahtar sözcükler: Havada Kapasitif Mikroişlenmiş Ultrasonik Çeviriciler, Dairesel CMUT, MEMS, Toplu ögeli model, Eşdeğer devre modeli, Doğrusal(DA) Yüklemesiz Operasyon, Yüksek Verim.

Acknowledgement

Contents

List of Figures

List of Tables

Chapter 1

Introduction

Airborne ultrasonic applications usually demand high acoustic power and wide bandwidth. Thin radiating plates must be employed in capacitive micromachined ultrasonic transducers (CMUTs) in order to obtain wider bandwidth in air. This is because the radiation resistance of air is very low and the mass of the plate must be kept at a minimum for a given operating frequency. Thin radiating plates yield under atmospheric pressure if they are not supported by a counter balancing pressure in the gap. Otherwise, the plate gets in contact with the substrate under static pressure. Present practice for wide bandwidth is to equalize the gap pressure by means of an air passage to ambient medium, which can be possible with perforated back-plate [1], [2] or perforated front-plate [3], [4] structures. This equalization introduces a significant loss, which further increases the bandwidth at the expense of transduction efficiency. In [3], front plate was perforated and tethered at a few points and it is shown that there is almost 70 dB loss .

Since CMUTs with vacuum gap are highly efficient, it may be possible to obtain a high pressure amplitude in a small bandwidth using a relatively low voltage level. On the other hand, both high power transmission and a reasonably wide bandwidth are required in some airborne applications such as ultrasonic communication [5], parametric arrays [6], proximity detection and distance measurement [7], [8], biological scanning [9], shape reconstruction [10], and imaging [11].

There are many studies about fabrication, characterization and modeling of capacitive ultrasonic air transducers [12–17]. The first airborne CMUT is discussed in [12] which employed polymer membrane. The silicon micromachining technique for ultrasonic transducer production was further developed [13–17]. Thin metal, silicon [1], silicon nitride membrane [2] or polymer membranes [3], [4] are used with pressure equalized gap to achieve wide bandwidth. An alternative way to increase the bandwidth is to combine various CMUT cell sizes across the entire device [17], to provide a stagger tuning effect.

We provide an equivalent circuit model-based approach for a thorough analysis of an airborne transmitting CMUT cell. We derive and present the limits for bandwidth and power for the CMUT cell with evacuated gap and silicon plates, operating in elastically linear range. We report a design methodology to achieve high transmission performance, where the plate swings the entire gap height without collapse. Theoretical findings and designs are verified with measurement results of fabricated CMUTs.

We also present a novel CMUT production method which employs anodic bonding. We impose an air channel between the gap and the ambient medium and avoid vacuum development in the gap during the wafer bonding. Afterwards we removed the air from the gap and sealed the channel in a vacuum chamber.

Although, airborne CMUTs are typically analyzed and designed to operate in the linear region. The linear regime constraint defines a limit on the achievable lowest quality factor and therefore on the widest achievable bandwidth. The limitation of the quality factor can be overcome by using lighter and/or stiffer materials as the plate material [18] in which diamond is used as a CMUT plate material.

We present an approach to overcome this difficulty and analyze airborne CMUTs in nonlinear regime to obtain a wider operation band. It is shown that a wide bandwidth can be achieved by using silicon material as top electrode instead of using stiffer material such as diamond.

In Chapter 2, we present basic physical principles of circular airborne CMUT

cells and unavoidable effect of ambient pressure, operation region and compliance change specific to Airborne CMUT are defined. An equivalent circuit model of CMUT is defined in Chapter 3. The model is used to examine the widest achievable bandwidth without any loss mechanism with silicon plate for linear compliance regime. In addition, a design procedure for unbiased operation which provides almost full swing is proposed and a design of 85 kHz airborne CMUT is explained. Fabrication details of designed CMUT cells and their characterization to make an accurate performance analysis are given in Chapter 4. Chapter 4 also includes comparison of simulation results with free field pressure measurements. Prediction errors are explained and discussed in detail. Concluding remarks are given in Chapter 5.

Chapter 2

Physical Fundamentals of Circular Airborne CMUT Cells

2.1 Effects of Ambient Pressure

A cross sectional view of a circular airborne CMUT and its important parameters are shown in Fig. 2.1, where a is diameter of the CMUT, t_g is gap height, t_i is insulating layer thickness, and t_m is plate thickness.

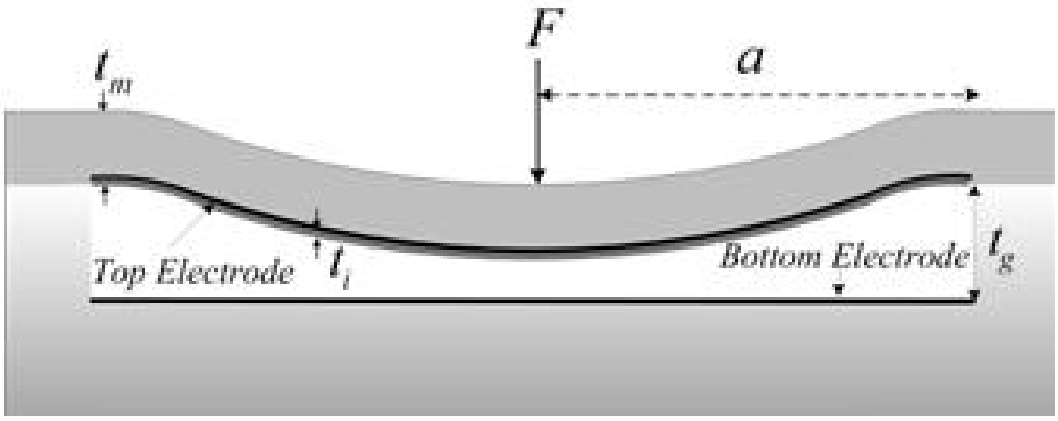

Figure 2.1: Cross sectional view of circular CMUT.

CMUTs have two electrodes as shown in Fig. 2.1. Top electrode is in the

movable plate and bottom electrode is placed on the substrate. Downward movement of top plate is limited with gap height. Driving this capacitive structure with electrical input signal moves the top plate and generates acoustic waves. Power of the generated waves depends on the plate swing. Larger swing produces larger acoustic power. Although increasing gap height seems to be the reasonable way of generating large acoustic power, CMUT with high gap requires high drive voltages. CMUT design involves computing of constraints on acoustic power and drive voltage. Our aim in CMUT design is to achieve high acoustic power while maintaining resonable drive voltage levels.

The important and unavoidable parameter in airborne CMUT design is external pressure. Atmospheric pressure depresses the plate towards the bottom plate which limits plate swing. Force induced due to atmospheric pressure is illustrated in Fig. 2.1 using F. We show that depressed plate produces higher power for a given voltage swing, despite the limited downward swing. However, we cannot depress the plate indefinitely since process imposes a limit. Over-depression may result in permanent collapse. Nevertheless, we can depress as much as the process allows. Also, depression level determines the operational behaviour of CMUT. Operational limits will be explained in the following section.

2.2 Elastic Linearity of Radiation Plate

The atmospheric pressure depresses CMUT top plate towards the bottom electrode. If the deflection is small, operation of a CMUT cell can be analyzed using a linear mechanical model. It is commonly accepted in literature that under 20 % of deflection to thickness ratio [19], a plate can be analyzed as it operates in linear region in terms of elasticity and above this point it is analyzed as it operates in nonlinear region. Hence, we assume that the dependence of pressure and deflection is linear if the center deflection, X_P, is less than approximately 0.2 of plate thickness [19], [20]. However, as the deflection is increased beyond this point, nonlinear effects in terms of elasticity become significant as shown in Fig. 2.2.

Fig. 2.2 is the result of finite element analysis (FEA) for silicon material. In Fig. 2.2 the dependency of deflection to thickness ratio, X_P/t_m, with respect to normalized pressure for silicon is depicted and the pressure is normalized by

$$\frac{Y_0}{(1-\sigma^2)}\left(\frac{t_m}{a}\right)^4 \tag{2.1}$$

where Y_0, the Young's modulus ratio, is kept to 130 GPa and Poisson's ratio, σ, is kept to 0.28 in FEA simulation. Silicon is a very flexible material and it is stiffened by static deflection. To observe the variation of stiffening effect for different radius to plate thickness ratios, a/t_m is varied between 10 to 200 while radius is kept to 200 μm. In the simulation, the applied uniform pressure is varied between 0 to 30 atm.

In FEA analysis, the nonlinear effects due to elasticity can be observed by enabling nonlinear simulation mode in which stress stiffening effect is considered. We generated Fig. 2.2 using both linear and non-linear modes. In the figure, blue lines corresponds to linear mode results while red line corresponds to nonlinear mode results. When a/t_m is increased, atmospheric pressure stretches the plate by deflecting it towards the bottom electrode. This deflection increases the stiffness of the plate.

Figure also shows that the difference between the linear and nonlinear becomes significant above the point that corresponds to 20% deflection ratio.

Under the same applied ambient pressure thick plate bends less compared to thin plates. As shown in Fig. 2.2 the thickest plate with $a/t_m = 10$ bends less than other plates under same ambient pressure. Although the simulation results between the linear and nonlinear modes are different from the beginning, the stiffening effect is considerable after 20 % of deflection to thickness ratio.

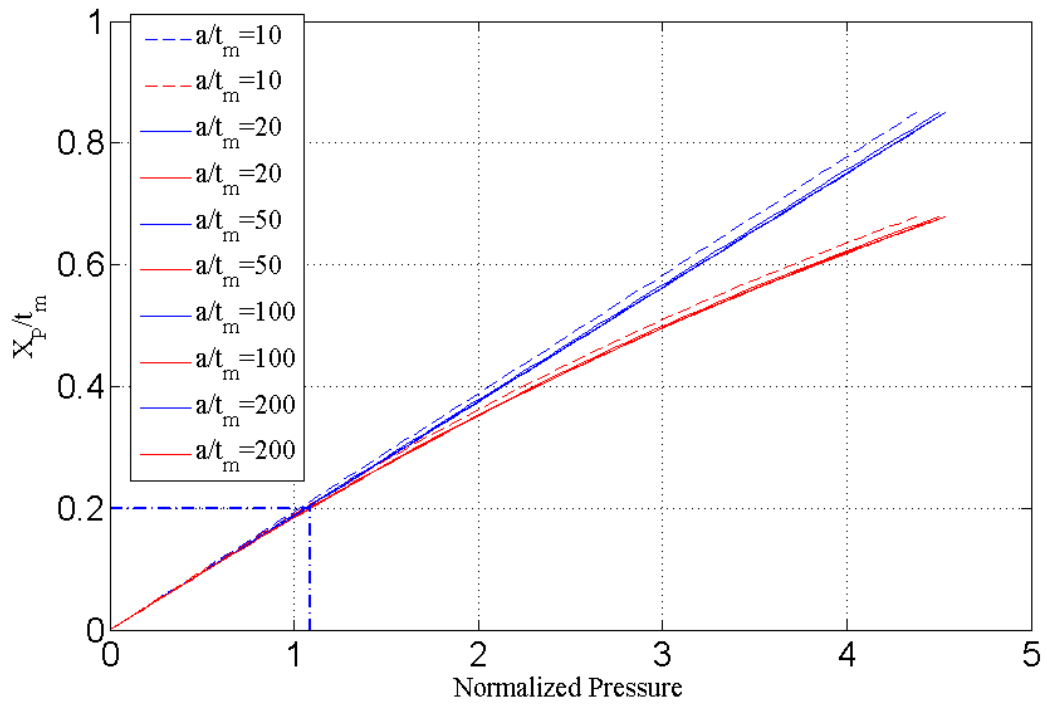

Figure 2.2: Deflection to thickness ratio versus normalize pressure for different a/t_m ratios.

2.3 Modeling the Stiffening Effect of CMUT Plate

The center deflection-to-thickness ratio may exceed 0.2 due to the atmospheric pressure. The stiffness of the plate increases and resonance frequency shifts upward. As a result, a relatively thin plate may act like a high stiffness material when it is deflected beyond its linear operation limits.

Downward shift in resonance frequency due to increase in a/tm ratio can be compensated by the increased stiffness of the plate. Therefore, higher a/t_m ratios, hence lighter plates are possible for the same resonance frequency. Designs in this range must consider the induced stress in the plate.

Note that single crystal silicon is a very flexible material and its fracture stress is around 7000-9000MPa [21]. This excellent property makes silicon suitable to be used as a plate material where the plate is stiffened by static deflection.

The stress induced by deflection due to atmospheric pressure and dc bias is maximum at the periphery of the clamped plate. Induced stress cannot be allowed to increase indefinitely because it causes material fatigue. In normal operation this maximum stress must be kept below a certain allowable level.

The compliance of the plate deviates from its linear value as the plate is stiffened. The variation of rms compliance, C_R, normalized to its unstiffened value, C_{Rm}, with respect to X_P/t_m is depicted in Fig. 2.3.

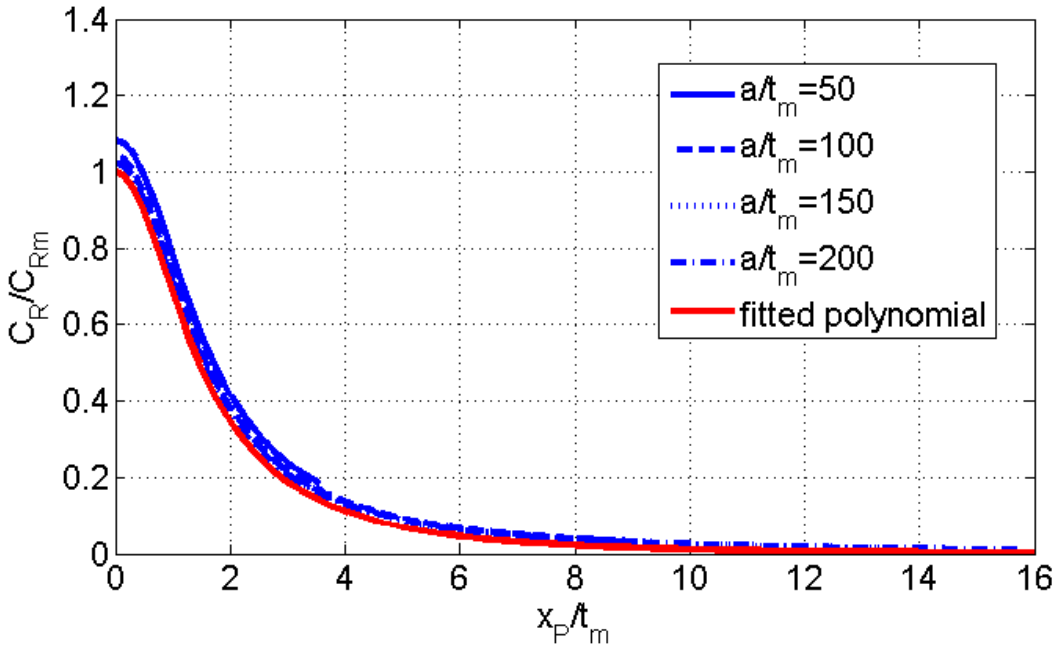

Figure 2.3: The ratio of average compliance to its unstiffened value with respect to deflection to thickness ratio.

C_R/C_{Rm} is obtained by FEA. a/t_m is varied between 50 and 200 and a uniform pressure between 0 to 30 atmosphere. Variation of C_R/C_{Rm} for different a/t_m values are depicted in Fig. 2.3. It is important to note that approximately the same variation with respect to X_P/t_m is obtained at all a/t_m values. Using this property the ratio of the rms compliance, C_R to unstiffened compliance, C_{Rm}, can be expressed with a polynomial as given,

$$\frac{C_R}{C_{Rm}} \cong \frac{1}{1 + 0.48|\frac{X_P}{t_m}|^2 - 0.014|\frac{X_P}{t_m}|^3 + 0.005|\frac{X_P}{t_m}|^4} \tag{2.2}$$

for $X_P/t_m < 12$ where X_P is the peak plate deflection. In Fig. 2.3, Equation (2.2)

is plotted with red line. When the plate is not deflected due to ambient pressure C_R/C_{Rm} should be equal to one which is in agreement with (2.2).

In order to avoid the singularity at the rim of clamped plate in FEA, we used a radius of curvature as depicted in Fig. 2.4. We select the radius of the curvature to be 3 μm. Maximum stress developed at the periphery is affected by the choice of this radius. Due to this curvature modification, FEA results have an error that is most observable at $X_P/t_m = 0$ as shown in Fig. 2.3. The difference is the largest for thick plate (at $a/t_m = 50$ the error is 8 %) and converges to zero as a/t_m increases.

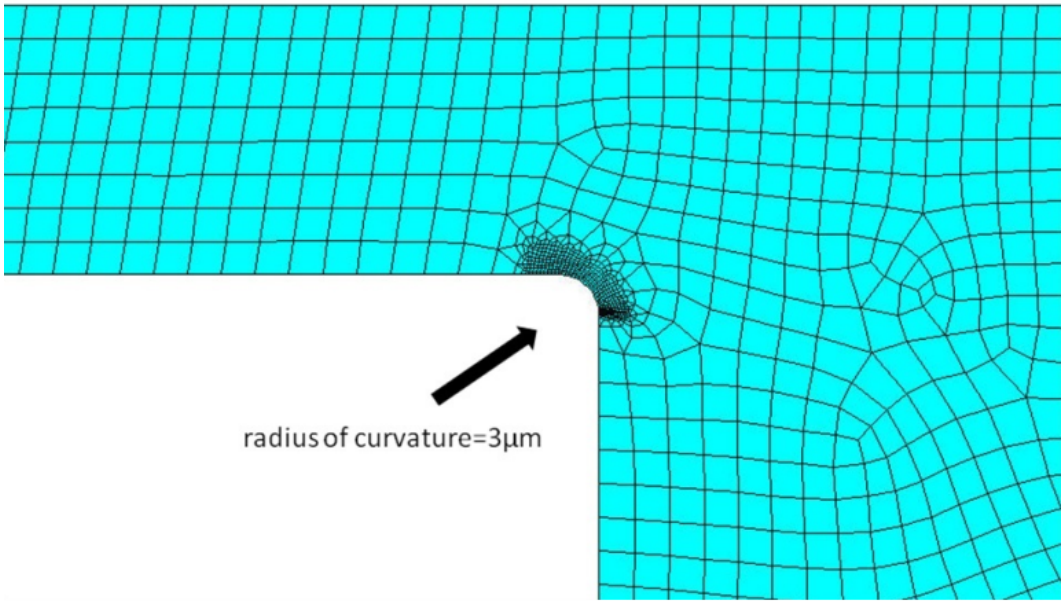

Figure 2.4: ka versus mechanical quality factor for different a/t_m values.

More depression results in stiffer plate. At $X_P/t_m = 4.6$ the plate is 10 times stiffer than that of unstiffened single crystal silicon plate. At $X_P/t_m = 7$ and at $X_P/t_m = 9.8$ the plate compliance are 20 times and 40 times stiffer than that of unstiffened single crystal silicon plate, respectively. Stiffer material is preferred because it results a wider bandwidth. Fig. 2.3 shows that there is significant nonlinearity change at $X_P/t_m = 4.6$ ratio. Although stiffer material causes wider bandwidth, we compromise to use this deflection to thickness point to reduce material fatigue.

The induced stress at the rim of a thin plate is proportional to the square of a/t_m ratio. The stress is multiplied by $(a/t_m)^2$ and plotted with respect to X_P/tm in Fig. 2.5 for a/t_m =50, 100 and 200. Multiplication by $(a/t_m)^2$ removes a/t_m dependency. The scaled curves approximately overlap with each other for all a/t_m ratios.

The figure shows that for $X_P/t_m = 4.6$, $Stress * (a/t_m)^2 = 1.8 \times 10^7$. For $a/t_m = 150$, the maximum stress due to atmospheric pressure and dc bias is approximately 800 MPa at the periphery of the plate.

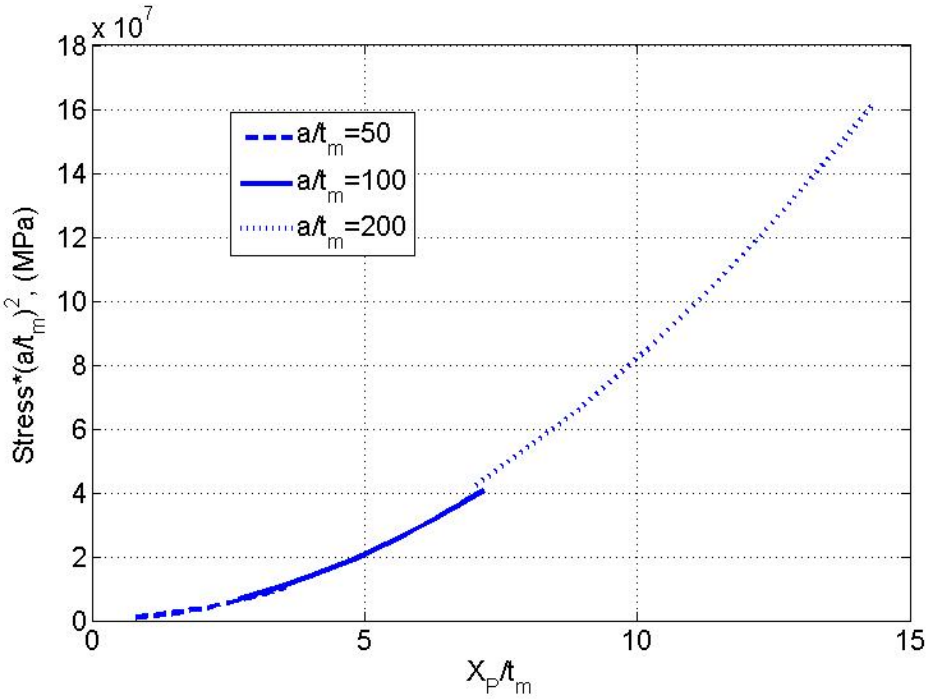

Figure 2.5: CMUT stress levels versus deflection to thickness ratio for different a/t_m values for a silicon plate.

Chapter 3

Operation of Airborne CMUT in Linear Compliance Regime

The basic geometry of a circular CMUT with a full electrode is given in Fig. 2.1. The displacement profile for thin clamped plates or membranes obtained using plate theory [22], [23], when depressed by uniform pressure, is

$$x(r,t) = x_p(t)\left(1 - \frac{r^2}{a^2}\right) \quad \text{for} \quad r \leq a \tag{3.1}$$

where a is the radius of the aperture, r is the radial position, and x_P is the displacement at the center of the plate; positive displacement is toward the bottom electrode. It is shown that CMUTs with full electrodes, with thin plate membranes, have the same profile [24]. The capacitance, $\delta C(r,t)$, of a concentric narrow ring on the plate of radius r and width dr can be expressed as

$$\delta C(r,t) = \frac{\varepsilon_0 2\pi r dr}{t_{ge} - x(r,t)} = \frac{\varepsilon_0 2\pi r dr}{t_{ge} - x_p(t)\left(1 - \frac{r^2}{a^2}\right)^2} \tag{3.2}$$

where ε_0 is the permittivity of the gap and $t_{ge} = t_g + t_i/\varepsilon_r$ is the effective gap height. Here, t_i and t_g are the thicknesses of the insulating layer and the vacuum gap height, respectively, and ε_r is the relative permittivity of the insulating material. The capacitance, $C(t)$, of the deflected plate with full electrode can be found by an integration:

$$C(t) = \int_0^r \delta C(r,t) = C_0 g\left(\frac{x_p(t)}{t_{ge}}\right) \tag{3.3}$$

where

$$C_0 = \varepsilon_0 \frac{\pi a^2}{t_{ge}} \tag{3.4}$$

and the function $g(\cdot)$ is defined by

$$g(u) = \frac{\tanh^{-1}(\sqrt{u})}{\sqrt{u}} \tag{3.5}$$

$$g'(u) = \frac{1}{2u}\left(\frac{1}{1-u} - g(u)\right) \tag{3.6}$$

$$g''(u) = \frac{1}{2u}\left(\frac{1}{(1-u)^2} - 3g'(u)\right) \tag{3.7}$$

Suppose we choose the rms plate velocity defined by

$$\upsilon_R(t) = \frac{\mathrm{d}x_R(t)}{\mathrm{d}t} = \frac{\mathrm{d}}{\mathrm{d}t}\sqrt{\frac{1}{\pi a^2}\int_0^a 2\pi r x^2(r,t)\mathrm{d}r} \tag{3.8}$$

as the through variable of the equivalent circuit, which is defined in [25] as the spatial rms velocity. For the plate profile in (3.1), we have $x_R(t) = x_P(t)/\sqrt{5}$. To preserve the energy, the corresponding across variable for force, $f_R(t)$, should be written as

$$f_R(t) = \frac{\partial dE(t)}{\partial dx_R} = \sqrt{5}\frac{\partial dE(t)}{\partial dx_P} \tag{3.9}$$

$$f_R(t) = \sqrt{5}\frac{C_0 V^2(t)}{4x_P(t)}\left[\frac{t_{ge}}{t_{ge}-x_P(t)} - \frac{\tanh^{-1}\left(\sqrt{\frac{x_P(t)}{t_{ge}}}\right)}{\sqrt{\frac{x_P(t)}{t_{ge}}}}\right] \tag{3.10}$$

3.1 Large Signal Equivalent Circuit

The circuit variables on the electrical side can be found by considering the time rate of change of the instantaneous charge, $Q(t) = C(t)V(t)$, on the CMUT capacitance:

$$\frac{\partial Q(t)}{\partial t} = C(t)\frac{\partial V(t)}{\partial t} + \frac{\partial C(t)}{\partial t}V(t) = i_{Cap}(t) + i_V(t) \tag{3.11}$$

similar to the notation in [24]. Hence, the current components are

$$i_{Cap}(t) = C(t)\frac{dV(t)}{dt} = C_0\frac{dV(t)}{dt} + i_C(t) \tag{3.12}$$

where

$$i_C(t) = (C(t) - C_0)\frac{dV(t)}{dt} \tag{3.13}$$

The velocity current is given by

$$i_V(t) = \frac{\partial C(t)}{\partial t}V(t) = \frac{\partial C(t)}{\partial x_R}\frac{\partial x_R}{\partial t}V(t) \tag{3.14}$$

We can form the large signal equivalent circuit as depicted in Fig. 3.1. C_{Rm} and L_{Rm} are the compliance of the plate and the inductance corresponding to the mass of the plate suitable for the $\{f_R,\ v_R\}$ rms model. For the same model, Z_{RR} is the radiation impedance of the CMUT cell, $Z_{RR}(ka) = R_{RR}(ka) + X_{RR}(ka)$, where $X_{RR}(ka) = \pi a^2\rho_0 c_0 X_1(ka)$ is the radiation reactance and $R_{RR}(ka) = \pi a^2\rho_0 c_0 R_1(ka)$ is the radiation resistance in air, where $X_1(ka)$ and $R_1(ka)$ are given in [24] for a clamped plate,

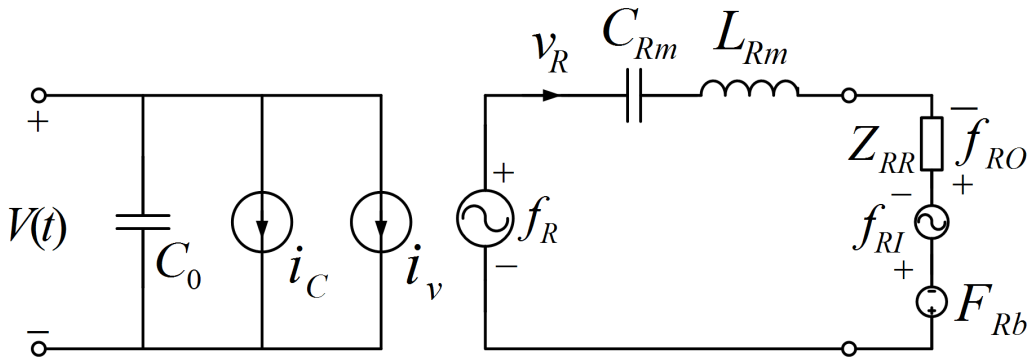

Figure 3.1: Large signal equivalent circuit referred to as the $\{f_R,\ v_R\}$ model, because the through variable in the mechanical section is v_R.

Because the direction of x_P is chosen toward the bottom electrode and the particle velocity of the acoustic signal propagating into the medium is in the opposite direction, we denote the polarity of the transmitted force, f_{RO}, across the radiation impedance, as shown in the figure. Similarly, any dynamic and static external force, such as an incident acoustic signal or atmospheric pressure, must appear in the form of f_{RI} and F_{Rb}, respectively, in the model.

For the velocity profile given by (3.1), the average velocity, $\upsilon_A(t)$, across the plate is equal to $\upsilon_A(t) = \upsilon_P(t)/3$. If $\upsilon_A(t)$ is the through variable, the across variable is $f_A(t) = 3f_R(t)/5$, which preserves energy in the f_A, υ_A model. Similarly, if $\upsilon_P(t) = dx_P(t)/dt$ is used as the through variable, $f_P(t) = f_R(t)/5$ is the force variable. In all cases, the mechanical circuit components must be scaled properly to be consistent and equivalent. The circuit components for all of these models are listed in Table 3.1.

Table 3.1: Relations between the mechanical variables of different models for the equivalent circuit given in Fig. 3.2, and turns ratio and spring softening compliance in the small signal model.

	RMS	Average	Peak
Model	$\{f_R,\upsilon_R\}$	$\{f_A,\upsilon_A\}$	$\{f_P,\upsilon_P\}$
f	f_R	$(3/\sqrt{5})f_R$	$(1/\sqrt{5})f_R$
υ	υ_R	$(\sqrt{5}/3)\upsilon_R$	$(\sqrt{5})\upsilon_R$
C_M	$C_{Rm} = \frac{9}{5}\frac{(1-\sigma^2)a^2}{16\pi Y_0 {t_m}^3}$	$C_{Am} = \frac{5}{9}C_{Rm}$	$C_{Pm} = 5C_{Rm}$
L_M	$L_{Rm} = \rho\pi a^2 t_m$	$L_{Am} = 9/5L_{Rm}$	$L_{pm} = 1/5L_{Rm}$
Z_R	Z_{RR}	$Z_{AR} = 9/5Z_{RR}$	$Z_{PR} = 1/5Z_{RR}$
f_I	$\pi a^2 p_{in}$	$(3/\sqrt{5})\pi a^2 p_{in}$	$(1/\sqrt{5})\pi a^2 p_{in}$
f_O	$\pi a^2 p_o$	$(3/\sqrt{5})\pi a^2 p_o$	$(1/\sqrt{5})\pi a^2 p_o$
F_b	$(\sqrt{5}/3)\pi a^2 P_0$	$\pi a^2 P_0$	$(1/3)\pi a^2 P_0$
n	n_R	$n_A = (3/\sqrt{5})n_R$	$n_P = (1/\sqrt{5})n_R$
C_S	C_{RS}	$C_{AS} = 5/9C_{RS}$	$C_{PS} = 5C_{RS}$

pin and po are the incident and transmitted wave pressures at the radiation interface, respectively.

To quantify the collapse phenomenon, we consider the circuit of Fig. 3.2 for the $\{f_P, \upsilon_P\}$ peak model to examine the static behavior under collapse conditions when an external static force F_{Pb} is present. We apply a voltage of V_{dc} to get the force F_P and the static displacement X_P.The static force equilibrium in the mechanical section can be written as

$$F_P + F_{Pb} = \frac{X_P}{C_{Pm}} \tag{3.15}$$

which yields

$$\frac{V_{dc}}{V_r} = \sqrt{\frac{3\left(\frac{X_P}{t_{ge}} - \frac{F_{Pb}}{F_{Pg}}\right)}{2g'\left(\frac{X_P}{t_{ge}}\right)}} \quad \text{for} \quad \frac{X_P}{t_{ge}} \geq \frac{F_{Pb}}{F_{Pg}} \tag{3.16}$$

where we define V_r as

$$V_r = \sqrt{\frac{4t_{ge}^2}{3C_{Pm}C_0}} = 8\frac{t_m}{a^2}t_{ge}^{3/2}t_m^{1/2}\sqrt{\frac{Y_0}{27\varepsilon_0(1-\sigma^2)}} \tag{3.17}$$

and $F_{Pg} = t_{ge}/C_{Pm}$ is the force required to deflect the plate until the center displacement reaches the gap height, $x_P = t_{ge}$.

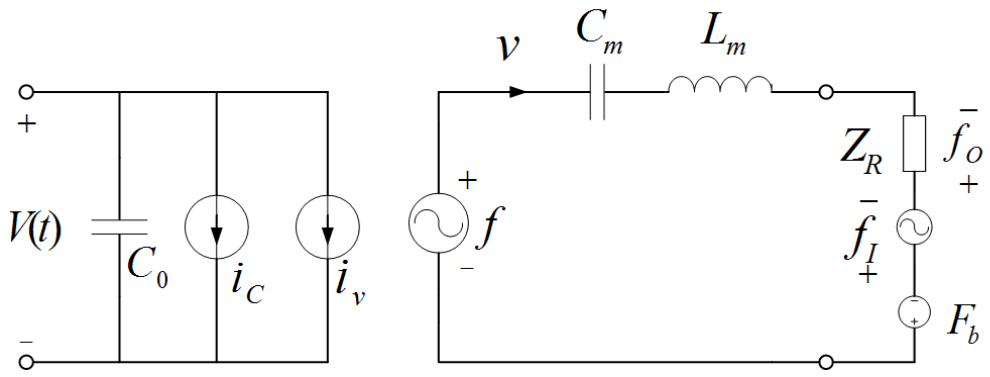

Figure 3.2: Generic large signal equivalent circuit model with parameters given in Table 3.1.

The displacement at collapse pointX_{Pc} can be readily evaluated from (3.16). For plates with full electrodes, a very accurate approximation is

$$\frac{X_{Pc}}{t_{ge}} \approx 0.4648 + 0.5433\frac{F_{Pb}}{F_{Pg}} - 0.01256\left(\frac{F_{Pb}}{F_{Pg}} - 0.35\right)^2 - 0.002775\left(\frac{F_{Pb}}{F_{Pg}}\right)^9 \tag{3.18}$$

The voltage, V_c, required to reach X_{Pc} can be obtained by using (3.18) in (3.16). The variation of V_c with respect to F_{Pb}/F_{Pg} is essentially a straight line and can be approximated as

$$\frac{V_c}{V_r} \approx 0.9961 - 1.0468\frac{F_{Pb}}{F_{Pg}} + 0.06972\left(\frac{F_{Pb}}{F_{Pg}} - 0.25\right)^2 + 0.01148\left(\frac{F_{Pb}}{F_{Pg}}\right)^6 \tag{3.19}$$

The low acoustic impedance of air does not allow wide-bandwidth designs for CMUTs with existing materials, although it provides a much wider bandwidth

compared to other transduction mechanisms. The mechanical quality factor of a single CMUT cell, Q_m, which can be derived from the equivalent circuit model, is given [26] as:

$$Q_m = \frac{\omega_r L_{Rm} + X_{RR}(k_r a)}{R_{RR}(k_r a)} = \frac{k_r a}{R_1(k_r a)} \frac{t_m}{a} \frac{\rho_m}{\rho_0} + \frac{X_1(k_r a)}{R_1(k_r a)} \tag{3.20}$$

where k_r is the wave number in air at the resonance frequency. The density ratio of plate material to air, ρ_m/ρ_0, is very high for typical micromachining materials. One of the suitable materials with relatively low density is single-crystal silicon , which is used in this thesis. For silicon the density, $\rho_m = 2370\ kg/m^3$, Poisson ratio, $\sigma = 0.14$ and the Youngs modulus, $Y_0 = 148$ GPa.

3.2 Lumped Element Nonlinear Circuit Model for a Circular CMUT Cell

A thinner plate is required to achieve a low quality factor level. However, atmospheric pressure deflects thinner plates more at high a/t_m ratios, causing increased plate stiffness due to nonlinear effects [26], [27].

The compliance of the plate deviates from its linear value as the plate is stiffened. Operation of a CMUT cell can be described using a linear mechanical model if the deflection is small. It is commonly accepted in the literature that for center deflection levels up to %20 of plate thickness, the system can be considered elastically linear [19].

Nonlinear dependence of the compliance on the deflection of the plate is explained in Section 2.3, where an FEA-based method to quantify this dependence is also given. Avery good approximation for $X_P/t_m < 12$ is given with (2.2). Plate compliance C_{Rm} is replaced with C_R in the equivalent circuit model for airborne applications.

3.2.1 Effects of nonlinearity in the compliance and force

The nonlinearities in the mechanical section of the airborne CMUT originate either from the compliance, C_R, or the transduction force, f_R. In the mechanical section, we have the following equilibrium relation:

$$f_R + F_b = \frac{x_R}{C_R} + (L_{Rm} + L_R)\frac{d^2}{dt^2}x_R + R_{RR}\frac{d}{dt}x_R \tag{3.21}$$

where $L_R = X_{RR}(ka)/\omega$ is the equivalent mass due to the radiation reactance around the operation frequency ω.

If the device is excited with high AC signal levels, the nonlinearity in the force term becomes dominant. The displacement dependency of the force term, $g'(u)$, can be expressed as:

$$g'(u) = \frac{1}{3} + \frac{2}{5}u + \frac{3}{7}u^2 + \frac{4}{9}u^3 + \sum_{m=4}^{\infty}\frac{m+1}{2m+3}u^m \tag{3.22}$$

where $u = x_P/t_{ge}$.

Using a Taylor series expansion around $u = 0$, it is clear that the coefficients of higher-order terms increase and converge to 0.5 for large orders. These terms are effective even for small normalized displacement levels.

Using (2.2), the restoring force term in (3.21) can be written as:

$$\begin{aligned}\frac{X_R}{C_R} \;\cong\; & \frac{t_{ge}}{\sqrt{5}C_{Rm}}u\left\{1 + 0.48\left(\frac{t_{ge}}{t_m}\right)^2|u|^2 - 0.014\left(\frac{t_{ge}}{t_m}\right)^3|u|^3\right. \\ & \left. +\; 0.005\left(\frac{t_{ge}}{t_m}\right)^4|u|^4\right\}\end{aligned} \tag{3.23}$$

The nonlinearity due to the second-order term in the compliance is studied both as simple spring constant behavior [20] and for its effect on the MEMS switch and resonators [28], [29]. It is shown that when the only significant nonlinear term in the dynamic force balance equation is the second term in the compliance, the resonance frequency shifts to higher values as the displacement amplitude increases. This effect is referred to as the Duffing effect [30]. However, as the

displacement amplitude increases, the nonlinearity in the force is also significant. This nonlinearity causes the resonance to shift to lower frequencies, because its effect opposes that of the compliance nonlinearity.

It is possible to study these effects in CMUTs quantitatively using the equivalent circuit model. The coefficient of the second-order nonlinear term in the compliance in (2.2), or the third-order term in the restoring force in (3.23), is $0.48(t_{ge}/t_m)^2$. The ratio t_{ge}/t_m is kept usually significantly smaller than unity in CMUT designs to avoid excessive bias and drive voltages. Therefore, $0.48(t_{ge}/t_m)^2$ is much smaller than the coefficient of the corresponding term in the transduction force in (3.22). The Duffing effect cannot be observed isolated from the nonlinearity in transduction force in CMUT designs where the t_{ge}/t_m ratio is small.

We studied the effect of nonlinearities for CMUT-I, the dimensions and critical parameters of which are given in Table 3.2, using an equivalent circuit and a commercial harmonic balance simulator, Advanced Design System, Agilent Technologies, USA [24].

Table 3.2: Dimensions of CMUTS used in the examples

		CMUT-I	CMUT-II
a	Plate radius (mm)	1.9	2.05
t_m	Plate thickness (μm)	80	80
t_{ge}	Effective gap height (μm)	6.4	6.4
t_i	Insulating layer thickness (μm)	1	1
V_r	Collapse voltage in vacuum (V)	646	558
F_b/F_g	Normalized exerted pressure	0.5 @ 1 atm	0.67 @ 1 atm
V_c	Collapse voltage for given normalized pressure (V)	308	172

CMUTs are usually operated with an AC voltage superimposed over a dc bias voltage [31–34]. The frequency of the ac voltage is in the vicinity of the resonance frequency of the CMUT in this mode for efficient operation.

Fig. 3.3 illustrates the operation of CMUT-I in this mode. We ignored the plate depression due to atmospheric pressure in these simulations in order to have

comparable results in prior studies [28–30]. The model is terminated by the radiation impedance of the CMUT in air, to avoid indefinitely large displacement amplitudes at resonance. The CMUT cell is biased at $0.8V_r$, and the sinusoidal signal amplitude, V_{ac}, is varied up to $0.00096V_r$, beyond which the CMUT collapses. It is clear that the frequency shift due to the force nonlinearity becomes visible even at very low ac drive levels. The peak center swing amplitude is only 0.76 μm at collapse threshold where the dc depression is 1.175 μm. The only loss mechanism to limit the swing amplitude at the resonance frequency is the radiation resistance, which is very low in air. Therefore, the collapse occurs at very low swing amplitude in biased operation. The swing increases for a lower bias voltage; however, the swing amplitude remains limited by the nonlinearity at all bias levels. This nonlinear effect has been studied as a limitation in MEMS resonators [29].

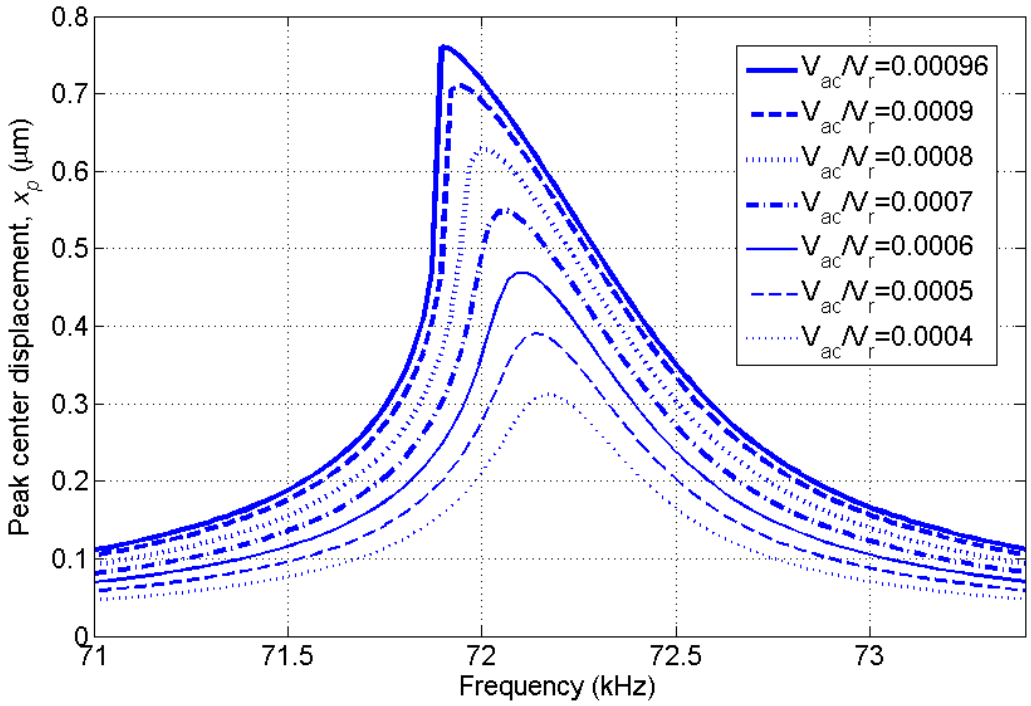

Figure 3.3: Calculated AC peak center displacement as a function of frequency for CMUT-I at different AC levels with a dc bias of $0.8V_r$ in vacuum.

3.3 Design Procedure for Large Swing in Unbiased Operation

3.3.1 Full Swing with Minimum Voltage Amplitude

3.3.1.1 Operation without Bias Voltage

CMUTs can also be driven without bias at half of the frequency of operation as:

$$V(t) = V_m cos\left(\frac{\omega t}{2}\right) \tag{3.24}$$

where ω is the radial frequency of operation [35], [36].

Fig. 3.4 shows the harmonic balance simulation results of CMUT-I for the unbiased mode when operated under 1 atm pressure. Increasing the drive amplitude lowers the resonance frequency and increases the displacement amplitude. The plate center is already depressed by 3.2 μm at 1 atm ambient pressure, and there is 2.95 μm clearance before the plate center hits the substrate. Part of this clearance is used by further static deflection due to the applied sinusoidal electric field, and another part by the sinusoidal swing of the plate. At the maximum swing of 2.46 μm, %83 of the clearance is utilized before the plate pulls in.

A large plate swing at low excitation voltage amplitude is an important design target for airborne transducers. Unbiased operation provides the option of reaching a swing amplitude which uses almost the entire remaining gap after static depression. We call this swing amplitude as full swing in this thesis. It is discussed in the following subsection that the full swing can be obtained at a certain frequency using a minimum drive voltage. We refer to this mode of operation as the Minimum Voltage Drive Mode (MVDM). The operating point of MVDM for CMUT-I is shown in Fig. 3.4.

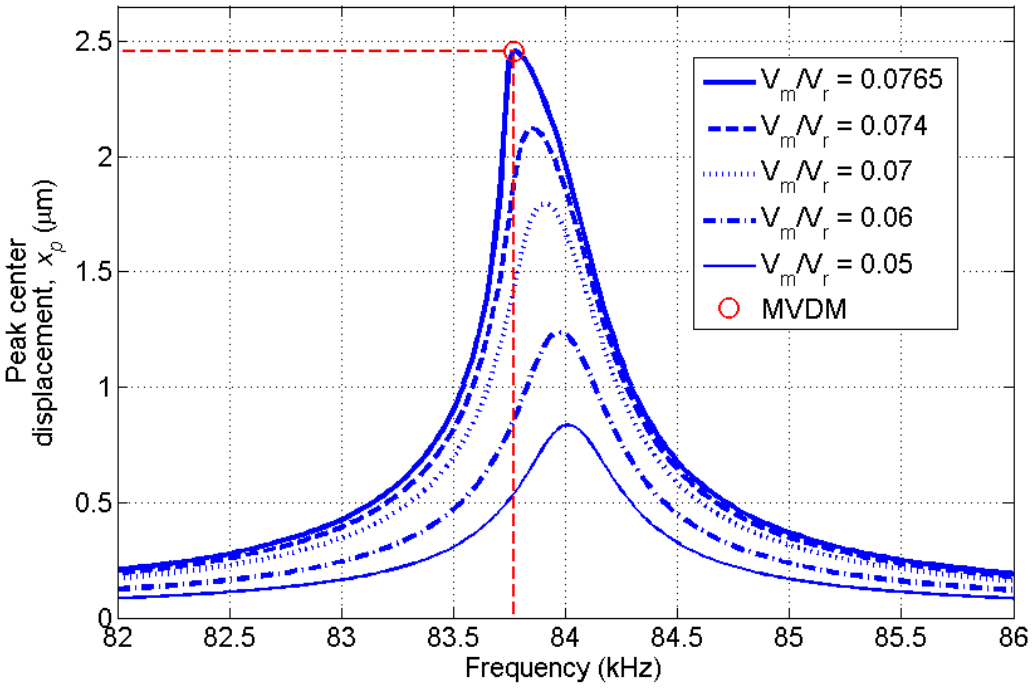

Figure 3.4: Calculated AC peak center displacement as a function of frequency for CMUT-I at different AC levels with a dc bias of $0.8V_r$ in vacuum.

3.3.1.2 Dependence of Swing and Collapse on Drive Amplitude and Frequency in Unbiased Operation

We fabricated CMUT-I and measured the free field pressure. The details and methodology of fabrication, the measurements and the differences between the fabricated CMUT and the design specifications are discussed in Sections IV and V.B, respectively. The free-field measurements of the emitted acoustic pressure at a 71.4 mm distance are given in Fig. 3.5a together with the calculated variation of the dynamic component of the center displacement of the plate in Fig. 3.5b.

It is important to note that the lowest frequency, 84.1 kHz, falls short compared to the MVDM frequency, 84.5 kHz, in achieving maximum pressure at a lower drive level. The simulation results given in Fig. 3.5b predicts MVDM at 83.7 kHz, where $0.5t_{ge}$ dynamic swing is achieved at $0.09V_r$ (58 V). A gradually decreasing swing can be obtained at higher frequencies, but at larger drive amplitudes.

The pressure increases in agreement with Fig. 3.5b until the center of the plate starts tapping the substrate, where pressure level saturates. The collapse event manifests itself as a tapping action in MVDM. A precise measurement of this phenomenon is difficult, since a large transient swing can interrupt the uncollapsed operation. There is an obvious difference of about %1 error between the designed frequency and realization. Furthermore, the maximum pressure is obtained in MVDM at a drive voltage of $0.14V_r$, compared to $0.09V_r$ in the simulation. The difference is due to the loss mechanisms of CMUTs, which are discussed and modeled in Section V. This loss also avoids collapse at the lower frequency of 84.1 kHz, and maximum swing is reached gradually, contrary to what is predicted by the lossless simulation.

The MVDM and its relation with the gap height is better understood when the variation of the total displacement, the sum of static and dynamic components, are examined. The calculated total center displacement normalized to effective gap height, t_{ge}, versus normalized drive voltage amplitude for CMUT-I is plotted in Fig. 3.6 for various frequencies. The maximum swing of the center is limited by the gap height. It is seen that a steady-state operation with full maximum swing, equal to t_{ge}, is possible. The maximum swing is achieved with lowest drive amplitude at 83.7 kHz.

The plate center is already depressed to $0.439t_{ge}$ by the atmospheric pressure, which can be seen as a starting point in Fig. 3.6. The swing extends across the entire effective gap as the drive level is increased for frequencies beyond 83.7 kHz. For CMUT-I, the free movement of the plate center is limited to $0.96t_{ge}$, the gap height, because of the insulating layer. This limit is also shown in Fig. 3.6. As the drive voltage is increased, dc displacement also increases and tapping starts when the total center displacement reaches $0.96t_{ge}$. The extra dc depression due to the drive voltage is only $0.021t_{ge}$ at MVDM.

The MVDM is a large signal operation. The harmonic component of the transduction force at MVDM frequency lags the velocity component by approximately 60° in CMUT-I, which is imposed by the mechanical LC section. The quadrature component of the force compensates this phase difference at MVDM

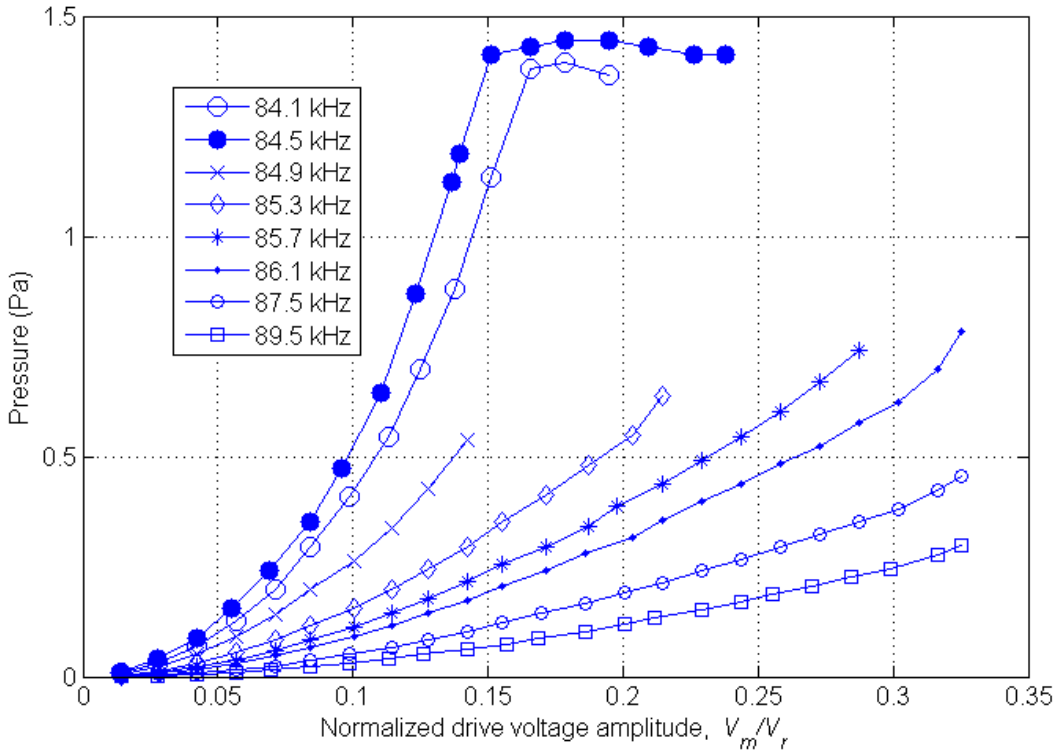

(a)

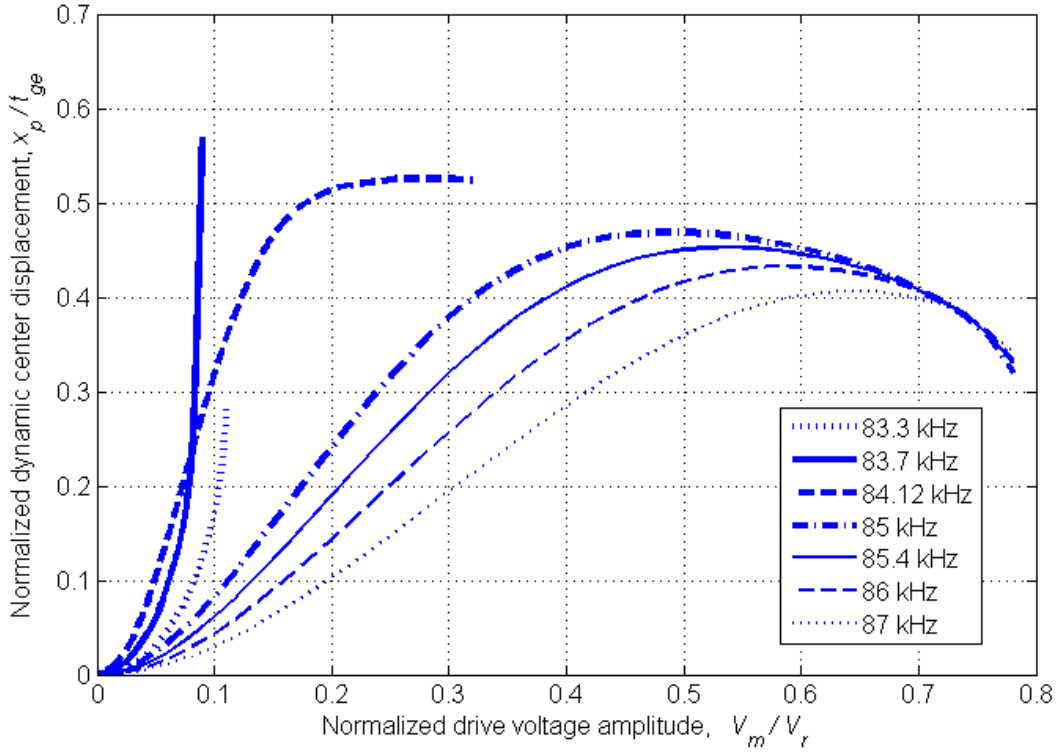

(b)

Figure 3.5: (a) Measured acoustic pressure for different drive levels at various frequencies near MVDM for CMUT-I; (b) Calculated normalized dynamic center displacement for different drive levels at various frequencies near MVDM for CMUT-I.

conditions, where the in-phase force component maintains the full swing against radiation resistance.

At a lower frequency, 83.3 kHz, the plate collapses at $0.11V_r$, where the dynamic part of the center displacement reach to only $0.281t_{ge}$. The maximum dynamic swing is less than that of MVDM and occurs at higher drive voltage amplitude. Fig. 3.6 shows that CMUT does not collapse, even for very high drive levels, at frequencies higher than MVDM frequency in unbiased operation if the insulator thickness, t_i, were zero. The swing gradually increases as the drive amplitude increases and approaches to t_{ge}. This phenomenon can be interpreted physically as follows: beyond MVDM frequency the mass of the plate appears as the main reactance that impedes the motion. The phase compensating quadrature force component is also inductive. The total impeding effect becomes more pronounced as the drive amplitude increases.

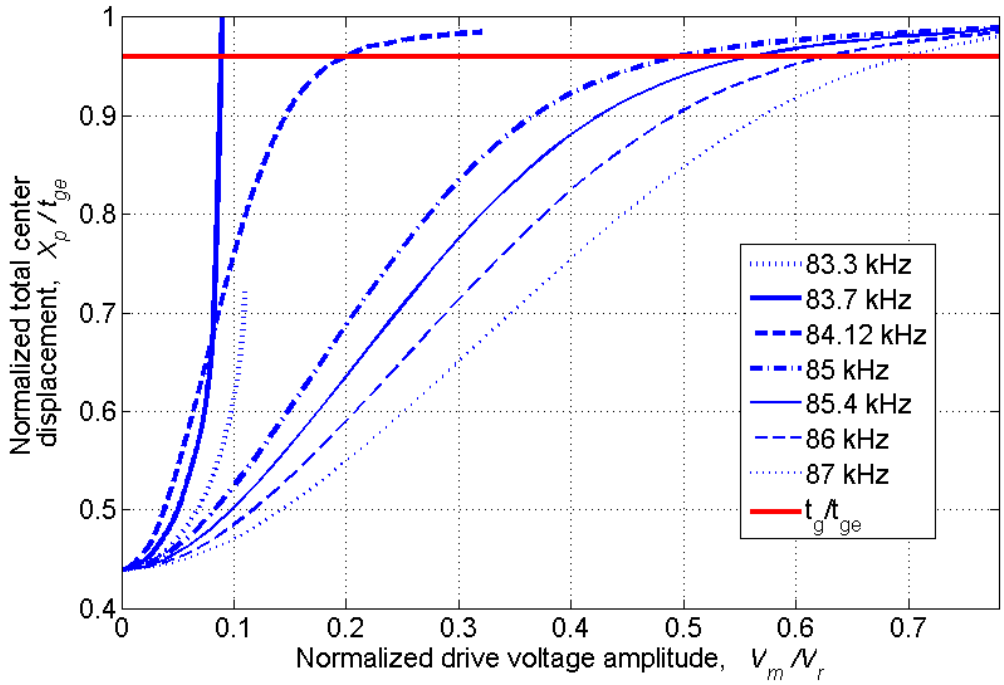

Figure 3.6: Calculated unbiased CMUT-I normalized total center displacement versus normalized drive voltages. The normalized gap height for tg=0.96tge is also shown.

3.3.2 Resonance Frequency

The plate resonates in air at a frequency in the vicinity of the unstiffened mechanical resonance frequency of the clamped elastically linear plate, when driven in MVDM. The mechanical resonance frequency can be obtained from the compliance and mass of the plate in terms of its dimensions and material properties. For example, the unstiffened resonance frequency of CMUT-I is 83.9 kHz, whereas the MVDM mode frequency is estimated as 83.7 kHz using the equivalent circuit model with stiffened compliance, C_R. Unlike the biased operation, there is not any pronounced spring softening effect in this mode. The resonance frequency is only very slightly pulled by the transduction force. The following relation between t_m/a, and $k_r a$ can be obtained at the unstiffened mechanical resonance frequency:

$$\frac{t_m}{a} = (k_r a) c_0 \sqrt{\frac{9}{80} \frac{(1-\sigma^2)\rho_m}{Y_0}} \tag{3.25}$$

3.3.3 Static Depression

Lower quality factors are achieved with thinner plates (higher a/t_m ratio), but thinner plates yield more under atmospheric pressure. This necessitates a deeper gap. The available normalized total displacement at the center of the plate is limited to:

$$\frac{X_{Pmax}}{t_{ge}} < 1 - \frac{F_{Pb}}{F_{Pg}} \tag{3.26}$$

for any depression level. The normalized depression level, F_{Pb}/F_{Pg}, can be expressed as:

$$\frac{F_{Pb}}{F_{Pg}} = \left(\frac{t_m}{t_{ge}}\right) \left(\frac{a}{t_m}\right)^4 \frac{3}{16} \frac{P_0(1-\sigma^2)}{Y0} \tag{3.27}$$

The depression depends on a/t_m and tm/t_{ge}. The depression level must be carefully specified at the design stage in order to (i) avoid unnecessarily high voltage levels and (ii) maintain elastically linear operation of the plate.

The maximum displacement of the plate center is limited to gap height, which can be taken as t_{ge}, approximately. Therefore, $t_{ge}/t_m < 0.2$ can be taken as the

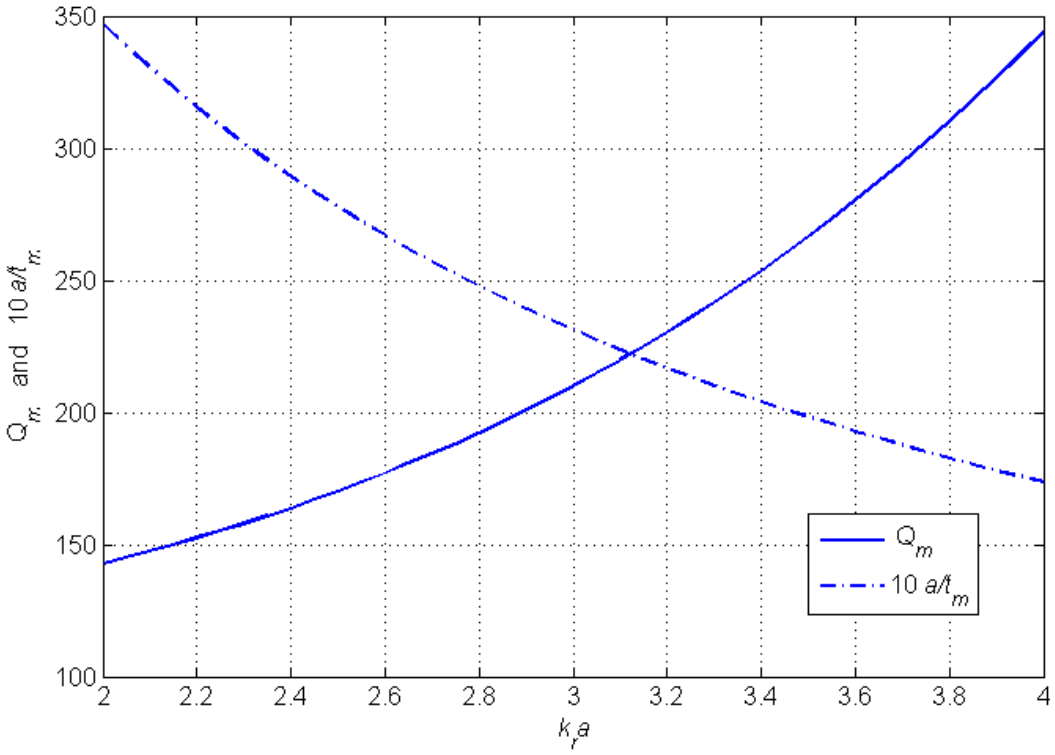

Figure 3.7: Calculated Q and a/t_m versus $k_r a$ for an airborne CMUT.

range for mechanically linear plate compliance. Using (3.25) in (3.27), we have:

$$\frac{t_{ge}}{t_m} = \frac{1}{(k_r a)^4 c_0^4 \rho_m^2} \frac{400}{27} \frac{Y_0 P_0}{(1-\sigma^2)} \left(\frac{F_{Pb}}{F_{Pg}}\right)^{-1} < 0.2 \tag{3.28}$$

which yields:

$$(k_r a)^4 \left(\frac{F_{Pb}}{F_{Pg}}\right) > 14.7 \tag{3.29}$$

for silicon in air under 1 atm. From (3.27) we also have

$$\frac{a}{t_m} = \left(\frac{16}{3} \frac{F_{Pb}}{F_{Pg}} \frac{t_{ge}}{t_m} \frac{Y_0}{P_0(1-\sigma^2)}\right)^{1/4} < 35.5 \left(\frac{F_{Pb}}{F_{Pg}}\right)^{1/4} \tag{3.30}$$

Q_m and a/t_m are shown as a function of $k_r a$ as calculated from (3.20) and (3.25) in Fig. 3.7. Inspection of these graphs indicates that a low quality factor requires a large a/t_m ratio at $k_r a$ values near 2. Smaller values of $k_r a$ cannot be used since static deflection is too high at those values. This imposes a lower limit for attainable Q_m. For example, the minimum $k_r a$ for linear compliance is 2.0 and 3.5 at $F_{Pb}/F_{Pg} = 0.9$ and 0.1, respectively. For these cases, we have $a/t_m = 34.6$ and 20.0, while $Q_m = 142$ and 265.

3.3.4 Design of 85 kHz Airborne CMUT

A CMUT cell for biased or unbiased operation can be designed using (3.20), (3.25), (3.26), (3.28) and (3.30). From (3.26), we know that a large F_{Pb}/F_{Pg} means a high static depression and leaves little room for dynamic movement. The static depression is large for thin plates, which provide larger bandwidth.

A design approach can be as follows:

1. Choose F_{Pb}/F_{Pg}.
2. Set an allowable value of $k_r a$ (smaller values give lower Q_m from Fig. 3.7) using (3.28) and determine t_{ge}/t_m.
3. At the chosen $k_r a$ value, determine Q_m and a/t_m from Fig. 3.7.
4. From the specified operation frequency, find a, t_m, t_{ge}.
5. Find the collapse voltage and check if it is less than the insulator breakdown voltage. If not, reiterate.

As an example, we design a CMUT cell at 85 kHz. We set a medium level of static depression by choosing $F_{Pb}/F_{Pg} = 0.5$. We choose $k_r a = 2.3$ for $t_{ge}/t_m = 0.2$ using (3.29). Fig. 3.7 gives $a/t_m = 29$ and $Q_m = 160$. Hence, we find $a = 1.46$mm, $t_m = 50\mu$m and t_{ge}=10μm. From (3.18) we find V_r=1055 V and from (3.16) we find collapse voltage, V_c, as 503 V. Since this value is above the dielectric breakdown voltage of our insulation layer, we start again with a larger value of $k_r a$. Using (3.28), we choose $k_r a3$ and $t_{ge}/t_m = 0.08$. Fig. 3.7 gives a/t_m=23.8 and Q_m=210. Hence, we find $a = 1.9$ mm, t_m=80 μm and t_{ge}=6.4 μm. For this case, $V_r = 646$ V and $V_c = 308$ V. This design is CMUT-I, the simulation and measurement results of which have already been discussed.

In order to increase the output power, we can consider increasing t_{ge} to the linear elastic limit, 16 μm, in CMUT-I for MVDM operation. When only the gap is increased, the static displacement remains the same and F_{Pb}/F_{Pg} becomes lower. Therefore, larger swing can be obtained at the expense of larger drive

voltage. The maximum displacement is reached in all tge values at the same normalized drive level of $V_m/V_c \approx 0.17$. This corresponds to 13.2 μm, 7.2 μm, 3.6 μm and 1.2 μm maximum swing at 353 V, 151 V, 59 V and 38 V drive amplitude for 16 μm, 10 μm, 6.4 μm and 4 μm effective gap height, respectively. The output field pressure is 11.3 dB greater compared to CMUT-I when the gap is 16 μm.

Another approach is to start by specifying the frequency and power delivered to the medium at the transducer surface. The required maximum dynamic displacement amplitude, x_{pmax}, can then be determined. It can be seen from Fig. 3.5b that a rather small extra static displacement occurs due to the applied voltage drive in the normal range of operation of MVDM. The normalized depression can be determined using required total displacement and (3.26).The radius can now be determined from (3.28). Having $k_r a$ specified, a/t_m, and hence t_m, can be found for a minimum Q_m. Since the normalized depression is also specified, tge is found from (3.27).

The precision of the fabrication processes is very important in realizing the designs to meet the specifications. In order to compensate for the fabrication tolerances, we fabricated eleven CMUT cells with radii ranging from 1.7 mm to 2.2 mm and with a fixed effective gap of 6.4 μm.

Chapter 4

Fabrication and Measurements

4.1 Fabrication

In this chapter, the fabrication process of designed CMUT cells, explained in Section 3.3, is described. A 80 μm thick, highly doped, double-sided polished silicon wafer is used as the plate and a 3.2 mm thick borosilicate wafer is used as the substrate of the CMUT. The thickness tolerance of the silicon wafer at the center is 8 μm and its five-point thickness variation is 10 μm.A 1 μm thick layer of silicon oxide is grown by wet thermal oxidation process on the silicon wafer in a diffusion furnace to form an insulation layer. For the electrical contact, the silicon oxide on one side is removed.

Cavities having a gap height of 6.4 μm are chemically etched on the borosilicate wafer, using buffered oxide etcher (BOE 7:1), as seen in Fig. 4.1a. Each gap is extended to the rim of the substrate by a 1 mm wide channel of same depth, to form a bed for electrical connection. 40 nm thick titanium and 100 nm thick gold layers are thermally evaporated on the bottom surfaces of the gaps to act as the bottom electrode, and on the bottom of the channels for electrical connection. To finalize the fabrication process, the wafer is anodically bonded (Applied Microengineering Ltd., Oxfordshire, UK).

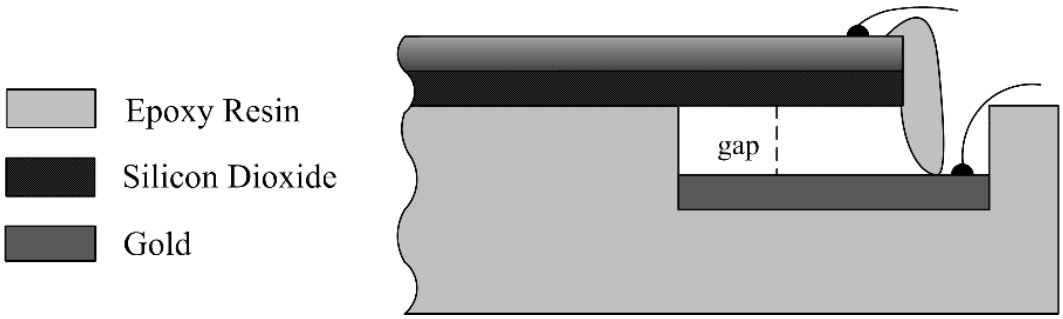

(a)

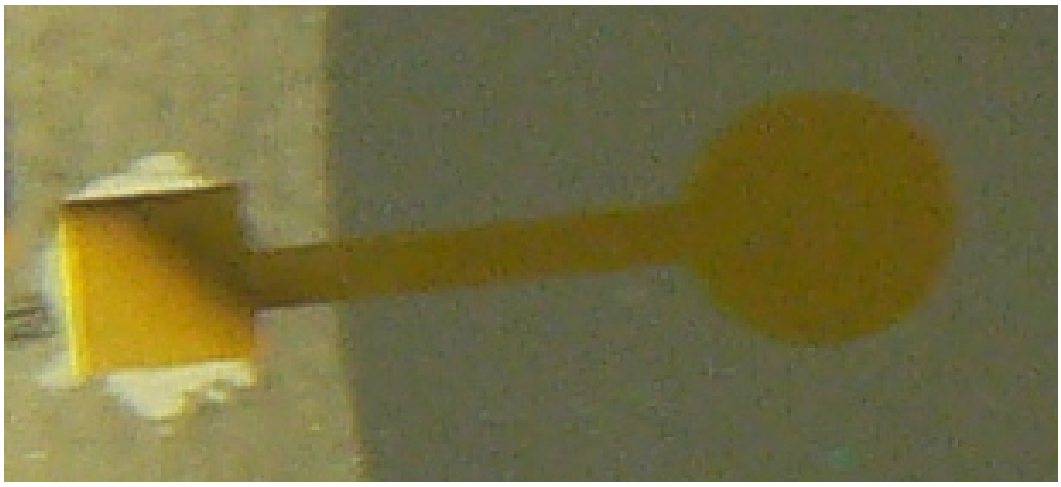

(b)

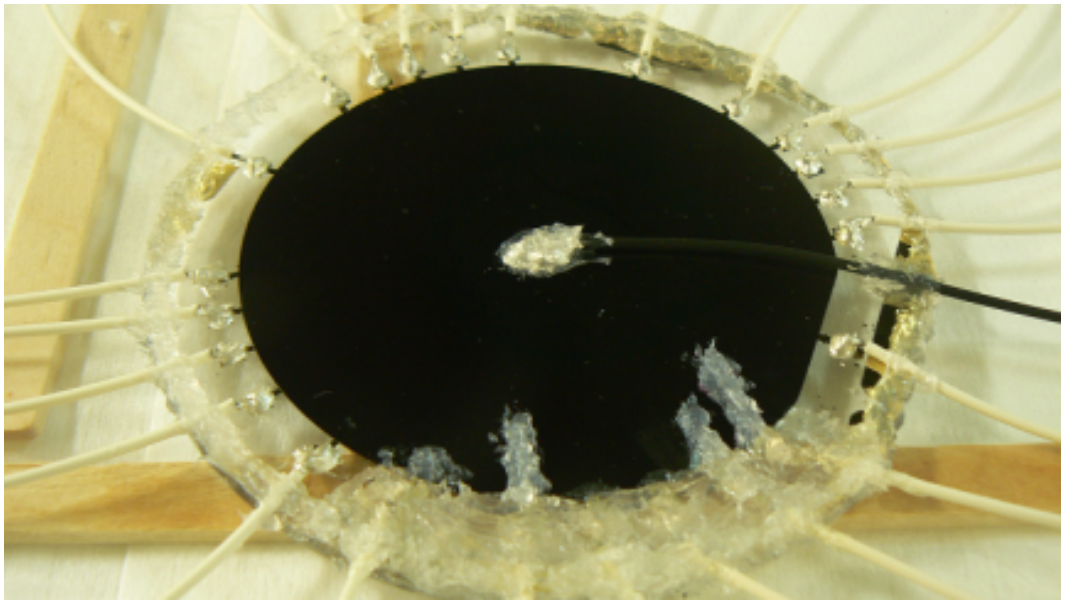

(c)

Figure 4.1: (a) Cross-sectional view of a fabricated single cell after anodic bonding, lead wire connections and epoxy; (b) Top (glass) view of a section with electrode (Ti-Au) of the fabricated CMUT; (c) Bottom (silicon) view of the fabricated CMUT.

The wafer is placed in a vacuum chamber to seal the channel by using a low viscosity epoxy resin (Sika Biresin CR80 epoxy resin and CH80-2 hardener).This way, the gas in the gap is sucked out through the epoxy. The wafer is left in the vacuum chamber at room temperature for 12 hours until the epoxy hardens. The wafer is then put in an oven at 70°C for 3 hours for curing.

We used an epoxy resin degassing desiccator and its vacuum pump as the vacuum chamber in our fabrication. The minimum pressure that can be obtained in this vacuum system is 0.12 atm. This finite pressure in the gap causes some deviation from the design parameters given in Table 3.1. However it also offers the possibility of testing our model based design and characterization approach which can handle this deviation once the pressure in the gap is known. Since CMUTs are operated at atmospheric pressure, the pressure difference causes a static deflection on the plate. The pressure in the gap is expected to increase since the gap volume is reduced by this deflection. However, we calculated that this pressure increase is insignificant for CMUT-II. The effective pressure on the is 0.88 atm at 1 ambient pressure, and F_{Pb} is calculated using this pressure difference.

The electrode channel also has the structure of a long rectangular CMUT with a width of 1 mm and a gap of 6.3 μm. We placed silicone rubber so as to cover the channel area on the plate surface in order to damp out any parasitic vibration, as can be seen in Fig. 4.1c.

We fabricated 3 wafers which have 24 CMUT cells each. Fig. 4.2 shows front view of one of the wafers. CMUT cells' radius are varied 1.7 mm to 2.2 mm by 0.05mm step size. CMUT cells' bending depth vary with radius even if the ambient pressure is the same. Therefore, CMUT cell fabrication with different radius allow us to examine the effect of initial depression depth due to static pressure.

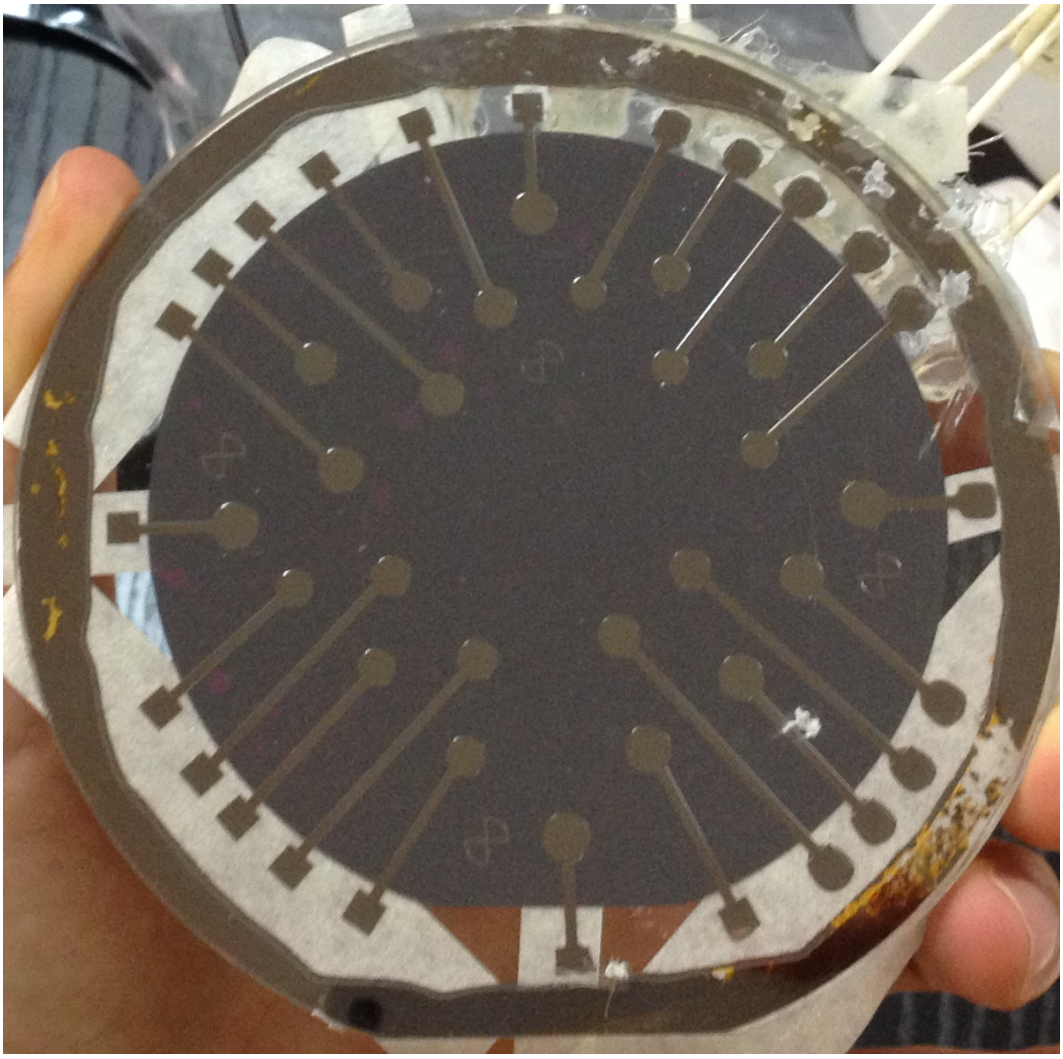

Figure 4.2: Front view of fabricated CMUT wafer that have 24 CMUT cells.

4.2 Characterization Using the Equivalent Circuit Model

We characterized the fabricated CMUT-II by measuring its electrical input impedance with an impedance/gain-phase analyzer (HP 4194A). The measurement is performed in *long averaging mode* with a bias voltage of 40 V. The equivalent circuit model is used to obtain the conductance of CMUT-II. The variation of conductance versus frequency is depicted in Fig. 4.3 for both the

measurement and the model. The model predicts a %2.2 lower resonance frequency, about twice as much peak conductance, no baseline conductance and about half as much bandwidth. The predicted quality factor is 190, whereas the measured value is 120. The discrepancies in these parameters may have to do with the validity of the assumptions about the material properties, the dielectric loss in the insulating oxide layer, or some of the dimensions such as gap height and plate thickness.

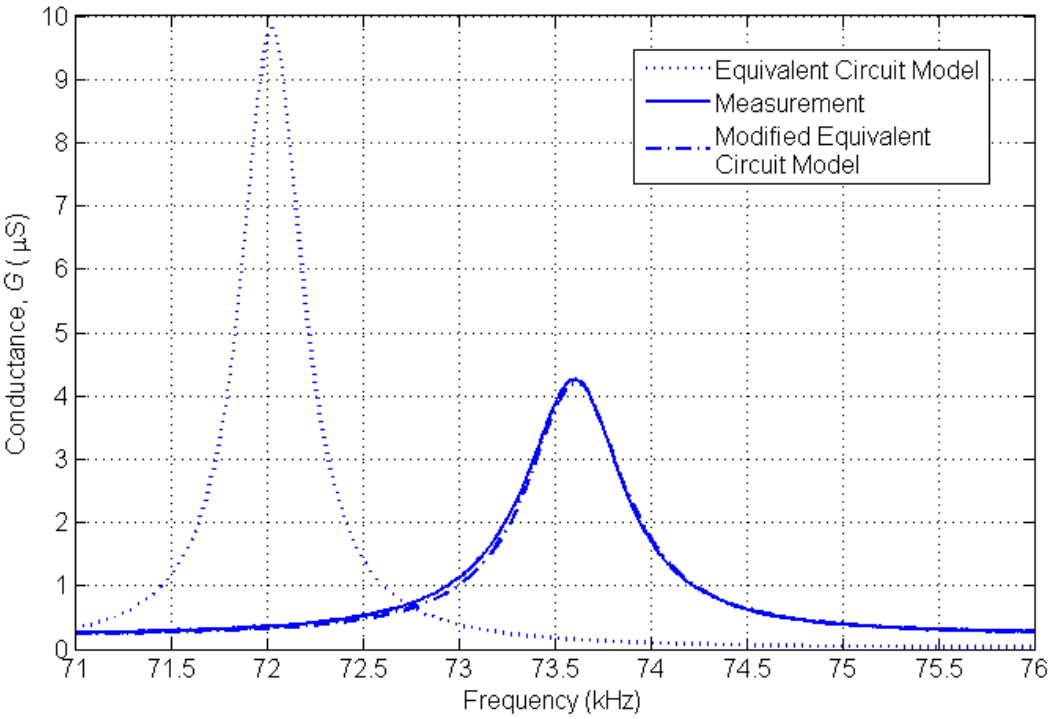

Figure 4.3: Conductance of the CMUT as measured and as calculated from the values found in fabrication.

We compensated for the discrepancies by making a few corrections in the model:

1. *Resonance Frequency*

   Mechanical resonance frequency depends on $L_{Rm}C_{Rm}$ and to the spring softening due to bias. $L_{Rm}C_{Rm}$ yields (3.25), which shows that the frequency depends on the square of radius, thickness and the mechanical material constants. Material constants we used in this work for single crystal silicon

are the most widely used values in literature. These constants are representative and can have a significant variation between different wafer samples. Hence we need not consider the effect of residual stress separately, both because it modifies the Youngs modulus additively and because it is usually few orders of magnitude low. It is not necessary to have the accurate knowledge of each of these variables in order to match the model to the frequency of resonance. The frequency is most sensitive to the radius, but we measure the radius quite accurately. Tuning the thickness to have (3.25) hold with the measured resonance frequency is most appropriate. The spring softening is affected by the gap height. The gap height also affects the peak conductance level. The spring softening effect can be ignored for initial frequency correction since the bias voltage is very low, and its effect can be checked after the entire tuning process is completed. The plate thickness is nominally 80 μm. To match the resonance frequency of the model and the measurement, we set the plate thickness to 81.63 μm.

2. *Conductance Baseline*

   In Fig. 4.3, the baseline in the conductance measurement is due to the loss tangent of the insulating layer. The dielectric loss of the oxide layers which we can produce in our laboratory is usually rather high. The effective loss tangent is calculated from the measurements as 0.0077. The total effective capacitance, $(C_0 + C_p)$, is obtained from the slope of the measured susceptance as 60.4pF. C_0 is calculated from (3.4) as 17.7pF, leaving a parasitic capacitance of C_p=42.7pF. The parallel effective dielectric loss resistance can be written as:

$$R_p = \frac{1}{\omega(C_p + C_0)tan\delta} \tag{4.1}$$

   C_p and R_p are connected in parallel with C_0 in the electrical side of the equivalent circuit model as depicted in Fig. 4.4

3. *Losses and Bandwidth*

   A certain amount of vibration energy is lost to the substrate. Since the plate motion is counterbalanced by the substrate, the loss can be modeled by an appropriate parallel impedance, Z_b, as shown in Fig. 4.4. We analyzed the

way Z_b affects the equivalent circuit by modeling the propagation into the substrate from the bottom surface of the gap. It is possible to show that Z_b is a very large effective mass, which cannot have any significant effect on the performance.

There are two other possible mechanisms of loss. The first one is due to the in-plane components of the vibration induced in the plate. When the plate vibrates, a certain amount of in-plane energy is coupled to the silicon wafer at its clamped edge. The other is due to the heat generated when air in the gap (0.12 atm) is compressed by the plate in every cycle. The components that model both of these loss mechanisms must appear as series resistances connected immediately after the transduction force in the equivalent circuit.

With $Z_b = \infty$, we calculate the combined equivalent loss resistance, using (3.20):

$$\frac{Q_{simulated}}{Q_{measured}} = \frac{R_{RR} + r_{loss}}{R_{RR}} \tag{4.2}$$

The bandwidth that is found from the equivalent circuit model is 387 Hz, whereas as measured it is 615 Hz. The loss resistance, $rloss$, is found from (4.2) as $0.68 S_0 c_0$.

4. *Peak Value of Conductance*

   Adjustment at the conductance peak is made by changing the effective gap height to 6.605 μm, which does not result in a significant shift in the resonance frequency. Hence any further modification in thickness, t_m, is rendered unnecessary. It must be noted that this value of plate thickness is not necessarily the actual thickness, but its combination with assumed material properties and CMUT dimensions provide accurate predictions of the fabricated CMUT performance parameters.

The operational parameters of CMUT-II, F_b/F_g, V_r and V_c, are changed to 0.54 @ 0.88 atm, 602 and 264, respectively, after these modifications.

We performed the same characterization on CMUT-I and we obtained 80.3 μm and 6.7 μm for plate thickness and effective gap height, respectively. We calculated the series loss as $0.86 S_0 c_0$. When we used these values in modified equivalent

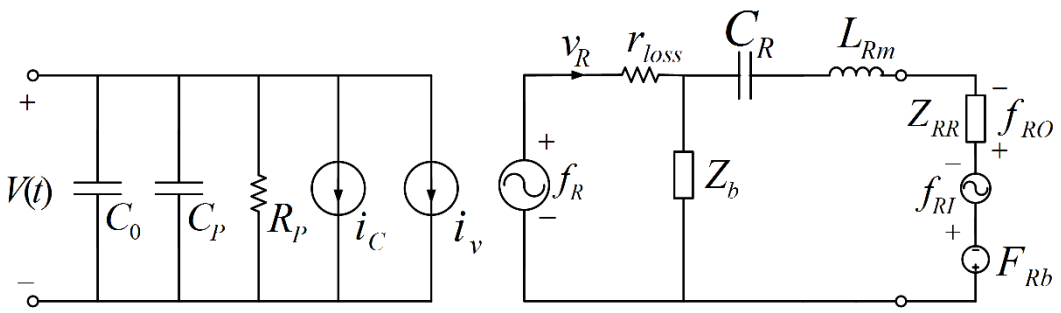

Figure 4.4: Modified equivalent circuit model of the CMUT.

circuit, we observed that MVDM occurs approximately at 84.2 kHz with drive amplitude of 90 V, which is $0.14V_m/V_r$, compared to $0.09V_m/V_r$ in the lossless model. This value is in exact agreement with the measurements in Fig. 3.5a.

4.3 Pressure Levels

A set of far-field measurements is made with CMUT-II. The field pressure is measured by using a calibrated microphone (1/8 in. pressure-field microphone, B&K 4138) placed at 90 degrees to the field [37], mounted on a preamplifier (B&K 2633) using a 1/4 in. adaptor (B&K UA 160). The microphone is polarized by a power supply (B&K Type 2807). A spectrum analyzer (HP8590L) is used to measure the preamplifier output voltage. The measurements are performed using continuous wave excitation in the laboratory environment where the setup is placed at least 1.5 m away from any reflecting surface and 2 m away from the ceiling. The measurements are made above 70 kHz, where attenuation in air is more than 2.2 dB/m [38]. Since the sound waves cannot persist with this level of attenuation, we did not observe any effects of reflected waves.

The microphone capacitance is given as 3.2 pF. We calibrated the measurement setup, from the 1/4 in. adaptor to the spectrum analyzer, using a 3.3 pF capacitor and a balanced 1 $\mathrm{mV_{rms}}$ voltage source.

Input signal amplitude is increased up to about 300 V peak or when collapse

occurs. The measurements were made in a laboratory where the ambient temperature and relative humidity were 18°C and %52, respectively. The ambient pressure was monitored and found to remain in the vicinity of 760 mmHg on all days when the measurements were made. The density of air, ρ, and velocity of sound, c, are taken as 1.204 kg/m^3 and 342.8 m/s, respectively. Attenuation in air in these ambient conditions and at the measurement frequencies is interpolated from the data given in [38]. The attenuation is less than 1 dB at the measurement distance of 250 mm and at 100 kHz.

The microphone is used to measure the acoustic pressure generated by the CMUT at a distance of 250 mm, for different normalized AC voltage values. To compare these results with the modified circuit model, we simulated the source sound pressure levels measured at 250 mm by using the equation given in [39]:

$$p(r,\theta,\phi) = j\frac{\rho c k S}{2\pi} D(\theta) U_A \frac{e^{-jkr}}{r} \tag{4.3}$$

where k is the wave number; r is the measurement range, 250 mm; $D(\theta)$=1, since the pressure is measured on the axis; U_A is the average velocity of the plate; and S is surface area.

Fig. 4.5 shows measurement results of fabricated CMUT-II output pressure levels at different frequencies together with the equivalent circuit simulator prediction for 73.7 kHz, the MVDM for this CMUT. There is a difference of about 4 dB between the model prediction and the measurements at all drive levels. There is a similar difference at other frequencies as well.

The CMUT can generate approximately 0.66 Pa (90.4 dB//Pa) at 250 mm in MVDM when driven by an amplitude of 71 V. The model predicts that collapse occurs at 96 V at this frequency. However, the collapse can occur prematurely at a lower drive level than predicted because the plate center can hit the substrate during the transient regime. This is observed in other frequencies, particularly at 74.1 kHz, where collapse occurred at a drive level lower than that of MVDM. The effect of attenuation in air on the measured values at MVDM is 0.55 dB [38].

The source level (SL) can be calculated as 78.9 dB//20μPa@1m, if attenuation is ignored. Therefore, one can obtain 118.9 dB SL if 100 similar cells are used in

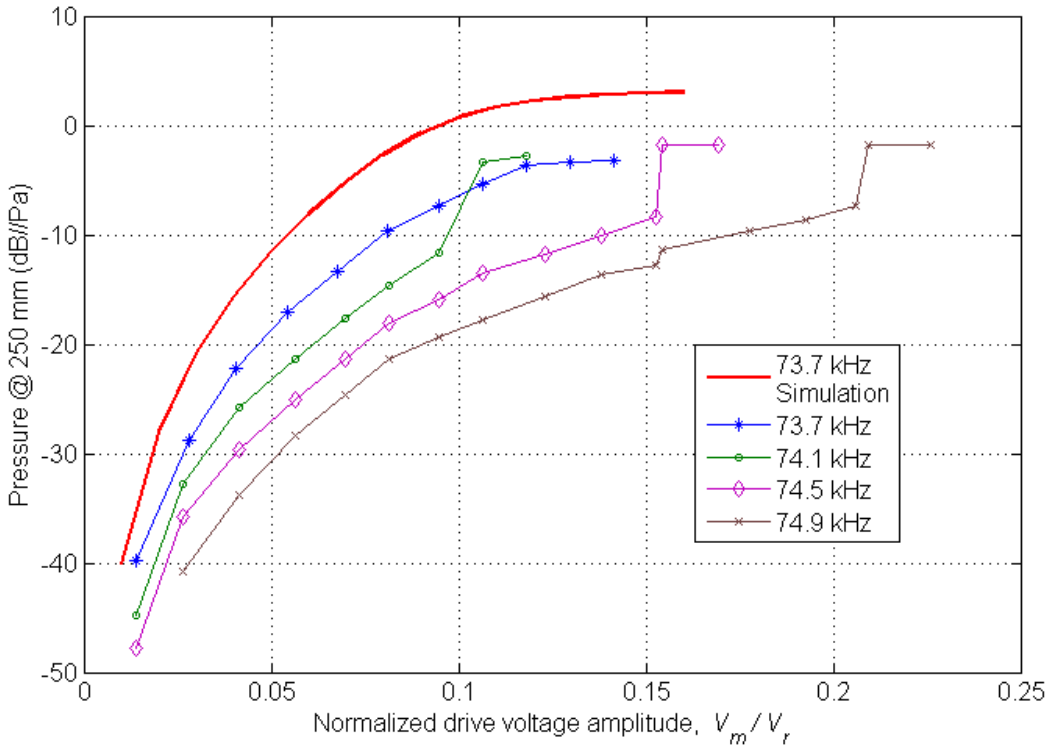

Figure 4.5: The pressure measurements of CMUT-II at various frequencies and driving voltages. Simulation predictions are given for MVDM at 73.7 kHz only. The simulation has the same discrepancy of 4 dB at other frequencies as well. CMUT-II pulls in at a normalized voltage amplitude of 0.12 @ 73.7 kHz; 0.11 @ 74.1 kHz; 0.16 @ 74.5 kHz; and 0.21 @ 74.9 kHz in the measurements.

a closed packed cluster.

In the simulator, we used (4.3) to calculate the source sound pressure level under the rigid baffle assumption. Another way to estimate the radiated pressure is to calculate the real power delivered to air at the acoustic port using radiation resistance and particle velocity, and assuming that this power is radiated omnidirectionally to the hemisphere. Radiated pressure levels thus obtained are 2.4 dB lower compared to the predictions of (4.3).

We tested twelve functioning CMUT cells in two steps: (i) impedance measurement and analysis and (ii) field pressure measurements. In eight of the cells we have a similar difference of 4-6 dB between the estimated and measured pressure levels. In four of the cells the difference is larger, but still less than 9 dB in

the worst case.

We investigated the mismatch between the predicted and measured field pressures

1. Instead of considering only the variation of tm and tge, we examined the variation of the radius, a, and the material properties of silicon in the characterization. The pressure generated at MVDM is not significantly affected by widely differing combinations, which yield the same impedance and the same MVDM frequency.

2. We considered the validity of the rigid baffle assumption in the model and the presence of other cells in the wafer, both experimentally and theoretically. We concluded that the rigid baffle assumption is appropriate.

3. There is a change in the displacement profile [40] when the cell is driven at high voltage levels, since the center approaches very near to the bottom electrode. The motion becomes more concentrated at the center and the beam-width becomes greater. We did not consider this change in the profile. The field pressure may be one or two dB lower when the change in profile occurs. This may account for the increased discrepancy at high voltage drive levels near pull-in.

We concluded that the differences between the measured and predicted pressure levels are due to an accumulation of the tolerances and minor inaccuracies of the measurement equipment and the setup. The free-field absolute pressure measurements are troublesome, particularly at high frequencies. These measurements are based on various assumptions and corrections [37]. A tolerance of a few dB is always in order.

4.4 Discussions

Time domain analysis of CMUT-II is also carried out using circuit simulator and result of the circuit simulator is given in Fig. 4.6. Transient response of CMUT-II

is also measured by vibrometer (Polytech OFV-5000) and plotted in Fig. 4.7.

In the experiment, we apply 1 V sinusoidal signal at 73.7 kHz using function/arbitrary waveform generator (Agilent 33250A) which is amplified by 10 times using a transformer. Although this voltage level results in small swing, we cannot increase the voltage amplitude due to limitations of our experiment setup. Output voltage is sampled with a sampling frequency of 200 kHz. This frequency is less than the Nyquist sampling rate, an accurate amplitude cannot be reconstructed accurately. However, envelope of the signal can be used for comparison with simulation results.

In vibrometer 1 V corresponds to 50 nm displacement and in steady state the dynamic displacement is calculated as 3.2×10^{-2} μm (Fig. 4.7) which is the same as the steady state response of the circuit simulator (Fig. 4.6). Measurement and circuit simulator results are in perfect agreement with low input voltage.

Acording to Fig. 4.7 transient response starts at %20 higher amplitude than its steady state value. These high transient oscillations cause early collapse that can be seen in Fig. 4.5 as jumps on the curve at 74.1 kHz, 74.5 kHz, 74.9 kHz.

In Fig. 4.8 displacement of the CMUT-II is visualized using the vibrometer.

There is a perfect agreement between vibrometer result and electrical circuit simulator prediction. The applied voltage in this experiment does not have high amplitude, therefore, Timoshenko's displacement profile is valid.

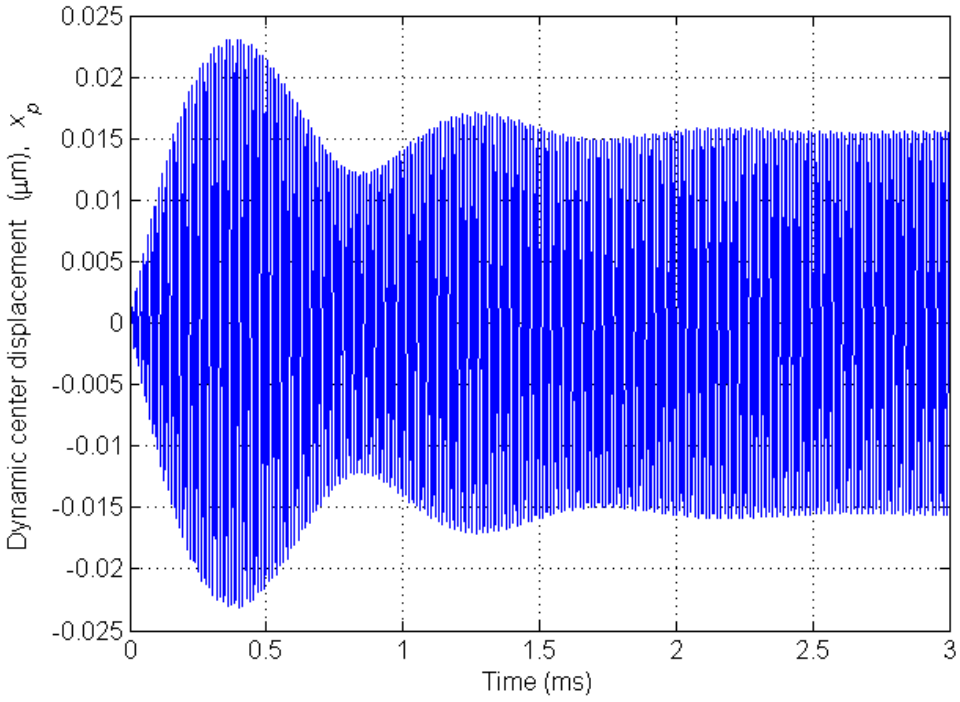

Figure 4.6: Transient response of equivalent circuit model in ADS at 73.7 kHz.

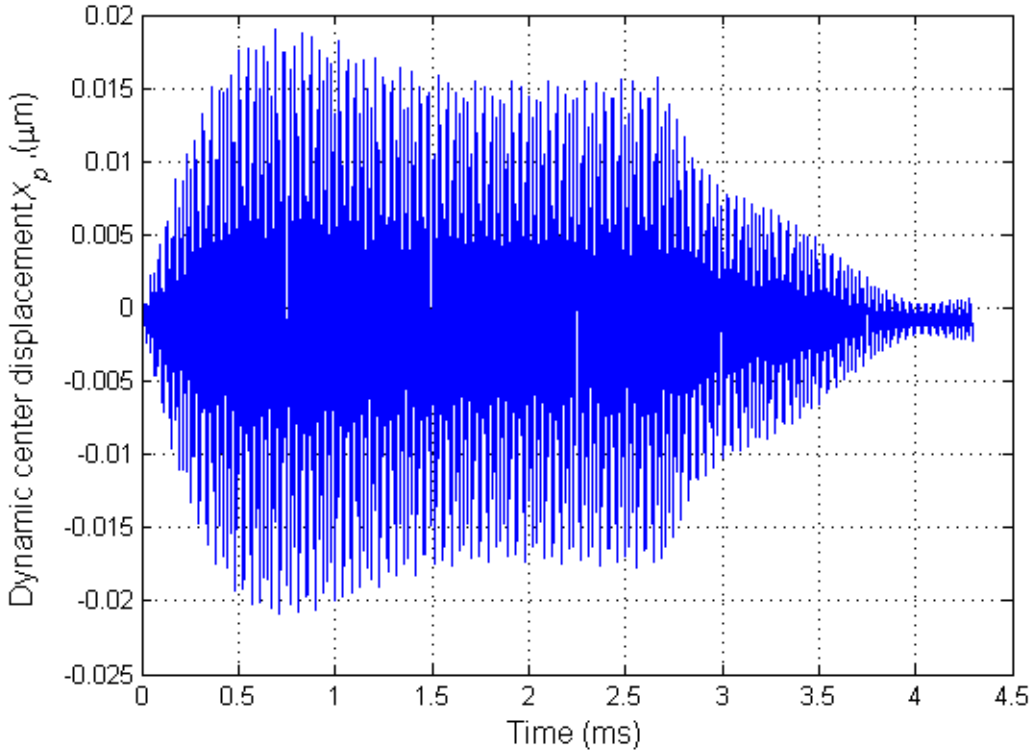

Figure 4.7: Transient response of the vibrometer at 73.7 kHz.

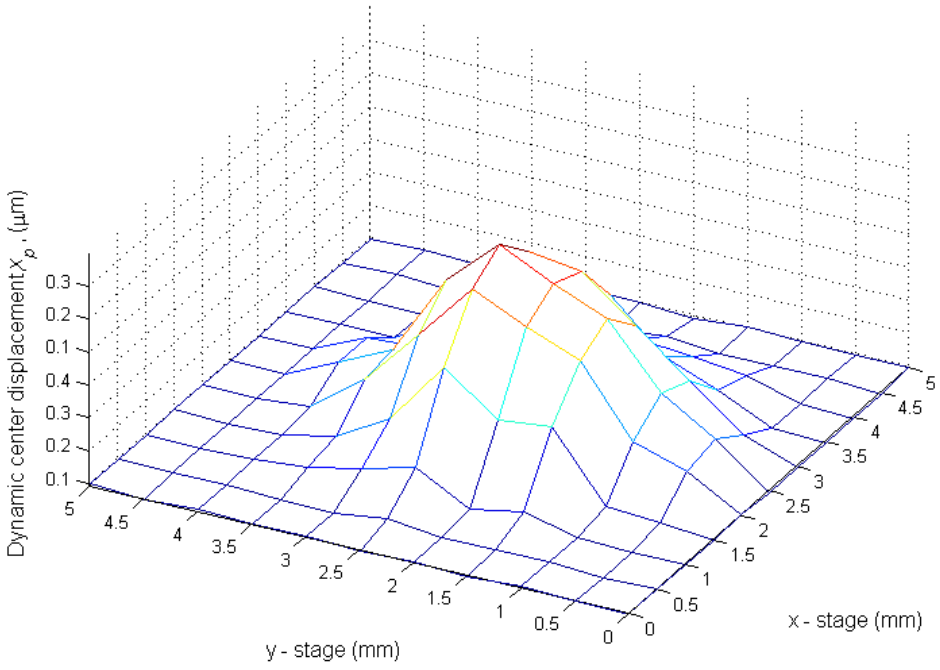

Figure 4.8: Visualization of the CMUT-II displacement at 73.7 kHz.

Chapter 5

Conclusions

In this work, an equivalent circuit model-based approach for a thorough analysis of an airborne transmitting CMUT cell is studied in elastically linear range. It is found that minimum quality factor of about 140 is achievable with silicon plates even at deflection levels close to the gap height. A method to obtain high pressure levels in airborne applications without any dc bias and using relatively low voltage amplitudes are presented. We identified a specific mode, MVDM, at which a CMUT produces maximum pressure using the lowest possible drive amplitude at a specific frequency. We presented a methodology for the design of airborne CMUT cells with maximum lossless bandwidth, which employs static atmospheric depression as a design parameter. We demonstrated how fabricated CMUT cells can be very accurately characterized using the equivalent circuit model.

To compare theoretical findings and designs with measurements, 3 wafers having 24 CMUT cells each are fabricated. We include the effect of ambient pressure in our theoretical analysis, therefore, fabricated CMUT cells have different radii to observe the initial depression depth effect on CMUT cell performance. We experimentally obtained 90.4 dB//20Pa@0.25 m pressure level at 73.7 kHz with CMUT-II using 71 V driving voltage amplitude, which corresponds to 78.9 dB SL. We showed that we can predict the performance very accurately during the design stage. Higher pressure levels can be obtained at the same frequency from

a single cell of the same area if a larger gap is employed with the same plate. For example, if the gap is increased from 6.4 m to 16 m in CMUT-II, the pressure level is increased by 11.3 dB.

It is shown that unbiased operation provides a specific mode, MVDM, which the full swing can be obtained at a certain frequency using a minimum drive voltage. Driving CMUTs at MVDM can be done similar to piezoelectric transducers, since the operation does not require any dc bias. At most a simple low-power transformer may be necessary whatever the voltage amplitude may be, since the MVDM is very efficient.

To make an accurate performance prediction of the fabricated CMUT cells, impedance measurement is used to modify the equivalent circuit model. There is a difference between predicted and measured resonance frequency and amplitude of the electrical input impedance. There are three main factors which cause this mismatch. One of them is the difference between the values of the material constants used in the fabrication and the constants used in the circuit model. The other reason is the difference between the dimensions used in the circuit model and fabricated dimensions due to imperfections in fabrication processes. The last factor may also be the residual stress in the plate, however, we do not consider the effect of residual stress separately. Because it modifies the Youngs modulus additively and it is usually few orders of magnitude low. Material constants we used in this work for single crystal silicon are the most widely used values in literature. To correct this difference we made corrections in the dimensions of the CMUT cell such as gap height and plate thickness within the tolerance range. As a part of the modification loss mecahanisms are also introduced in the electrical and the mechanical side.

The performance of the fabricated CMUT cells are predicted using modified equivalent circuit model. There is a difference between predicted pressure and measured free field pressure, and maximum observed error is 9 dB. We examine the reason of this difference and conclude that it is due to the change in the displacement profile. As CMUT cells are driven with high voltages, center of the plate reaches very close to the bottom electrode. And the profile deviates from

the Timoshenko's profile expression that is used in the circuit model. Our model cannot predict the performance of CMUT cells that are driven with high voltages. However, it perfectly predicts the performance of the CMUT cells that are driven low voltage amplitudes where the Timoshenko's displacement profile is valid.

Appendix A

Fabrication Details and Experimental Setup

As described in Section 3.4, CMUT cell gap and the electrode channel are etched till the same height. Therefore, we use only one mask in the fabrication process which is shown in Fig. A.1.

The mask is prepared to fabricate 11 CMUT cells with various radii to observe the static deflection effect on the performance of CMUT cells. Group A and Group B, each consist of 5 CMUT cells, illustrate the CMUT with the same radius. Group A has CMUT cells with radii ranging from 1.95 mm to 2.15 mm and Group B has CMUT cells with radii ranging from 1.7 mm to 1.9 mm. The rest 4 cells that are located on the edges of x and y axis have equal radius of 2.2 mm.

In the experiment, we tested 11 functioning CMUT cells in one wafer, 2 of them are defined in Chapter 3 in detail. Properties of other CMUT cells are given in Table A.1.

As a first step, to make an accurate performance prediction of CMUT cells, we modified the values used in equivalent circuit by matching simulated input electrical impedance with the impedances measured by impedance/gain phase

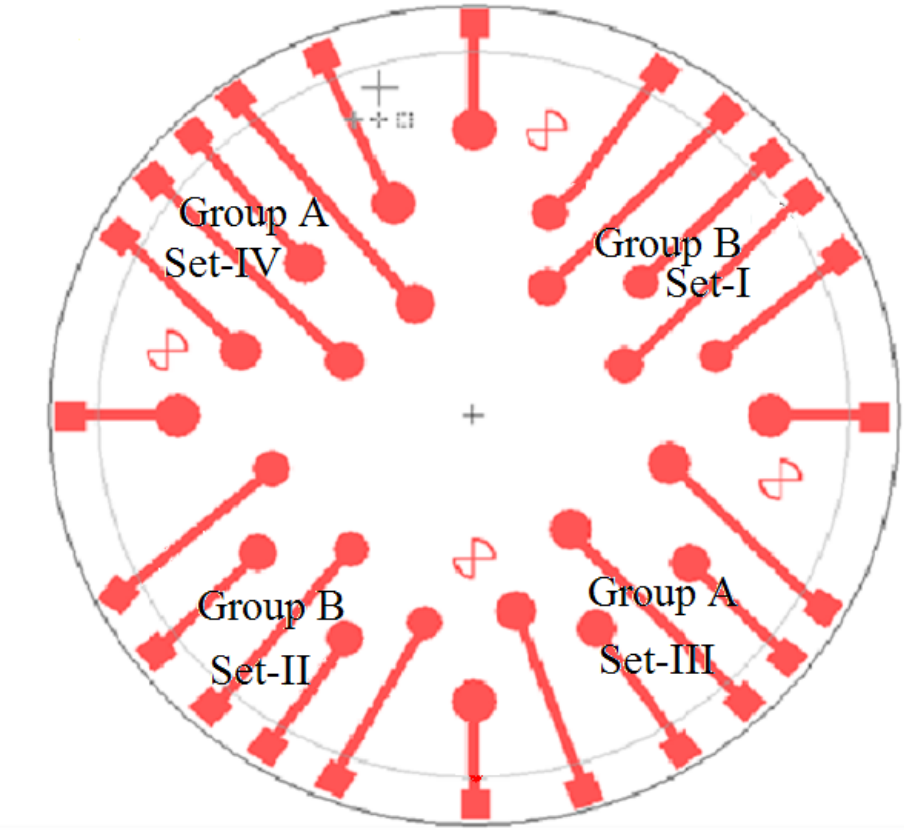

Figure A.1: Farication mask prepared in UNAM, Bilkent University.

analyzer (HP 4194A). These new dimension values (to compensate the difference between the measurement and the simulation) are also given in Table A.1. The measured input electrical impedance and simulation results by using modified equivalent circuit are shown in Figs. - .

Next, we performed the free field pressure measurements. The measurement equipments are shown in Fig. A.2. And the free field pressure results of CMUT cells defined in Table A.1 are given in Figs. - . Pressure levels are given in dB scale relative to 20 μPa

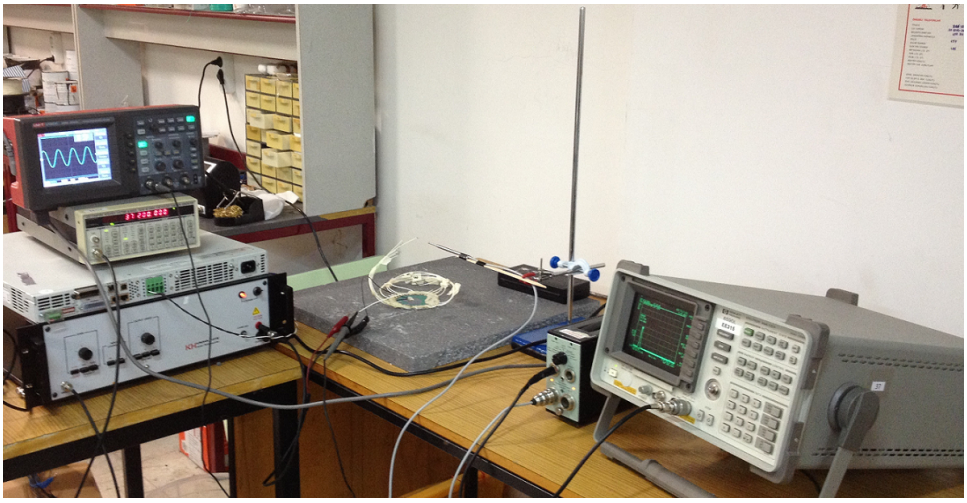

Figure A.2: The experiment set up used during the free field pressure measurements.

Table A.1: Dimensions of tested CMUTS.

CMUT	Set-II	Set-II	Set-III	Set-III	Set-III	Set-III	Set-IV	Set-IV	Set-IV
$a(mm)$	1.8	1.85	2.0	2.05	2.15	2.2	2.0	2.1	2.15
$t_m(\mu\text{m})$	77.3	76.95	78.18	81.85	81.3	84.9	78.6	80.65	83.2
$t_{ge}(\mu\text{m})$	6.685	6.75	6.633	6.525	6.52	6.232	6.682	6.758	6.59
$t_i(\mu\text{m})$	1	1	1	1	1	1	1	1	1
$V_r(\text{V})$	732	698	596	593	533	507	608	582	561
F_b/F_g	0.37	0.4	0.554	0.541	0.669	0.674	0.541	0.602	0.618
$V_c(\text{V})$	444	391	252	258	164	154	265	219	201

Table A.2: Description of variables used in Table A.1.

$a(mm)$	Plate radius
$t_m(\mu\text{m})$	Plate thickness
$t_{ge}(\mu\text{m})$	Effective gap height
$t_i(\mu\text{m})$	Insulating layer thickness
$V_r(\text{V})$	Collapse voltage in vacuum
F_b/F_g	Normalized exerted pressure @ 0.88 atm
$V_c(\text{V})$	Collapse voltage for given normalized pressure

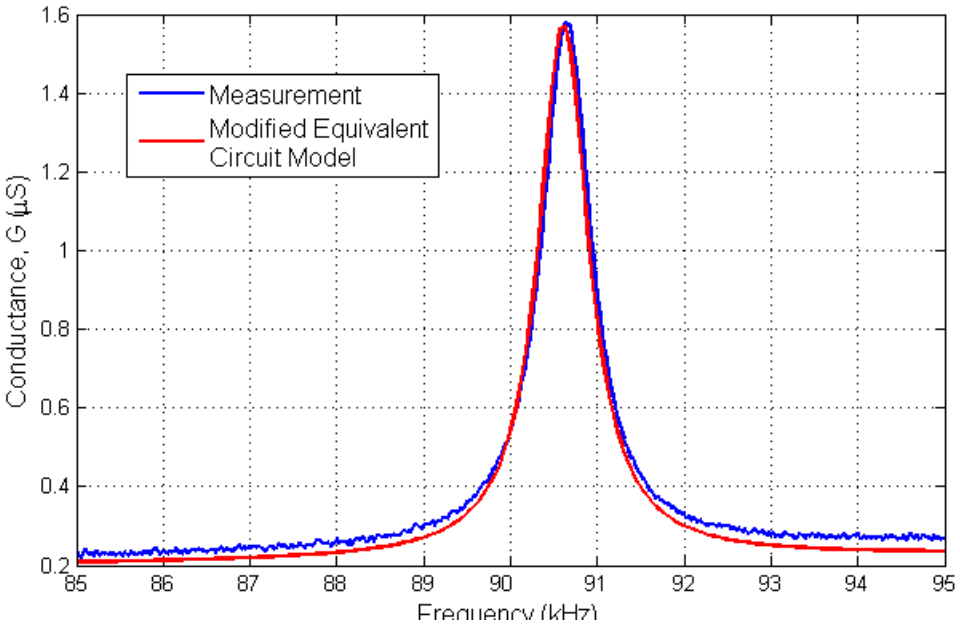

Figure A.3: Input electrical impedance of CMUT cell in set-II with a radius of 1.8 mm.

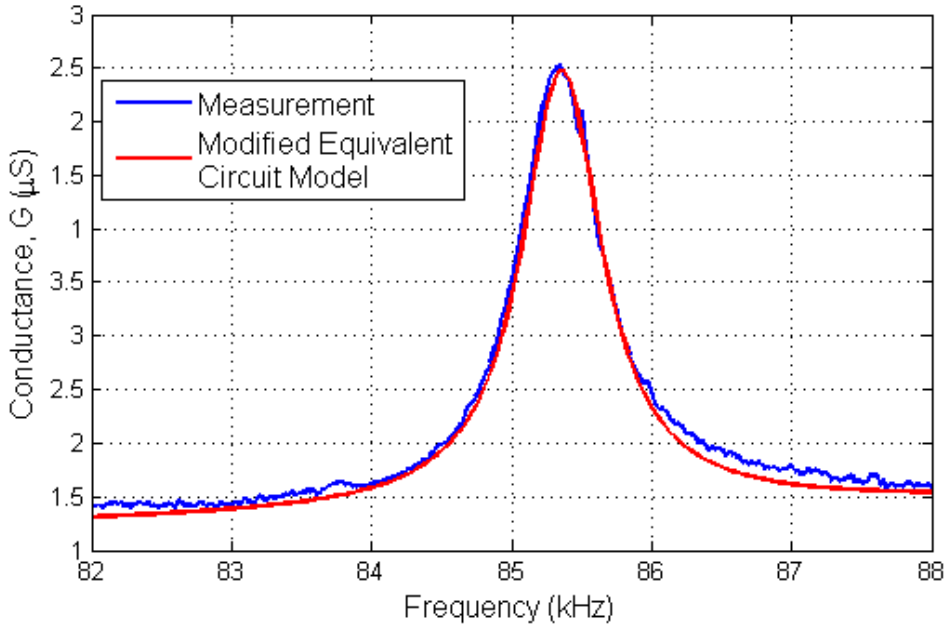

Figure A.4: Input electrical impedance of CMUT cell in set-II with a radius of 1.85 mm.

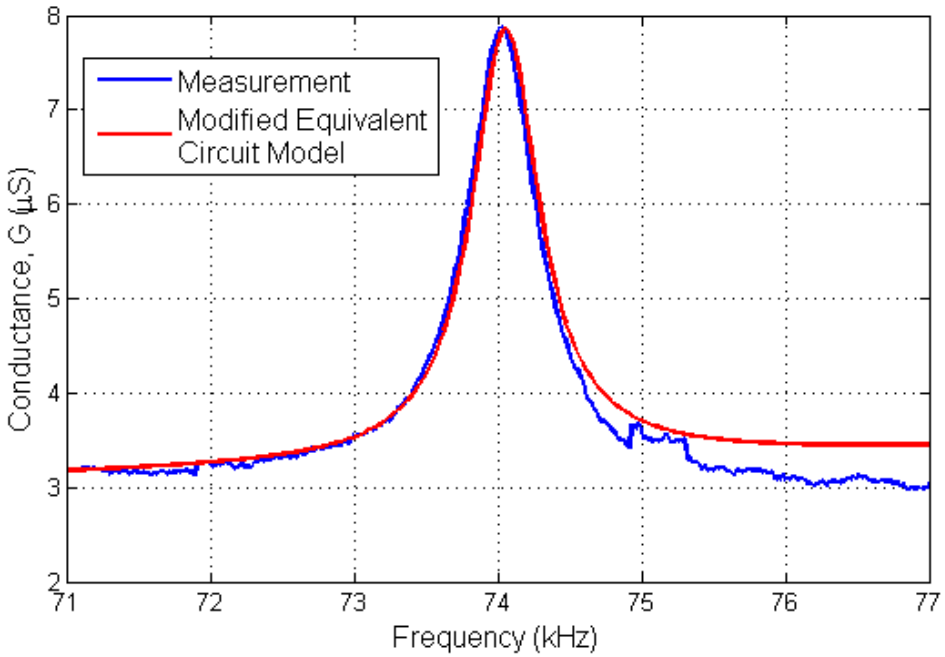

Figure A.5: Input electrical impedance of CMUT cell in set-III with a radius of 2.0 mm.

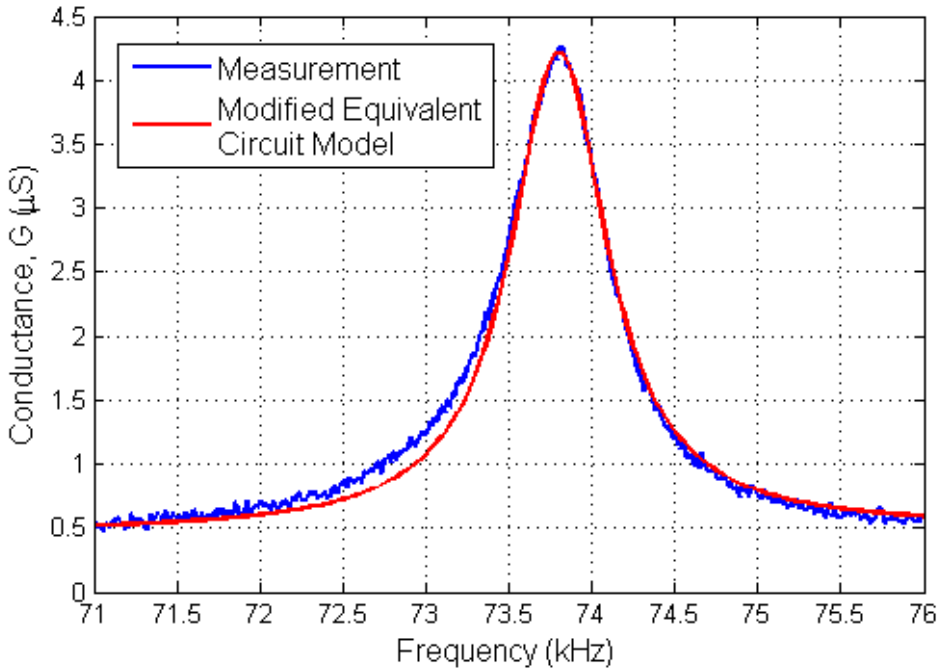

Figure A.6: Input electrical impedance of CMUT cell in set-III with a radius of 2.05 mm.

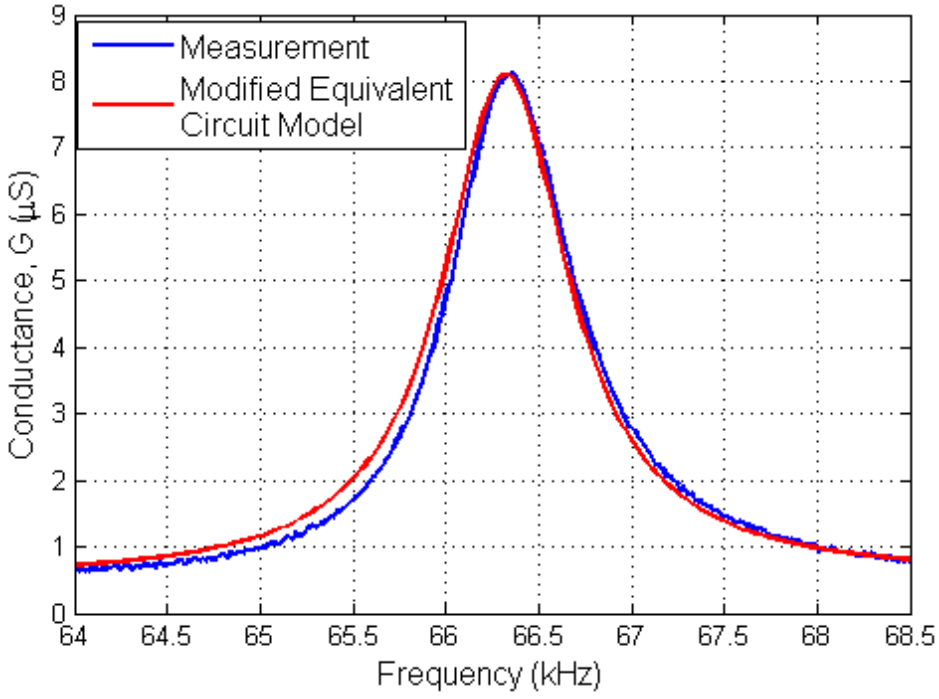

Figure A.7: Input electrical impedance of CMUT cell in set-III with a radius of 2.15 mm.

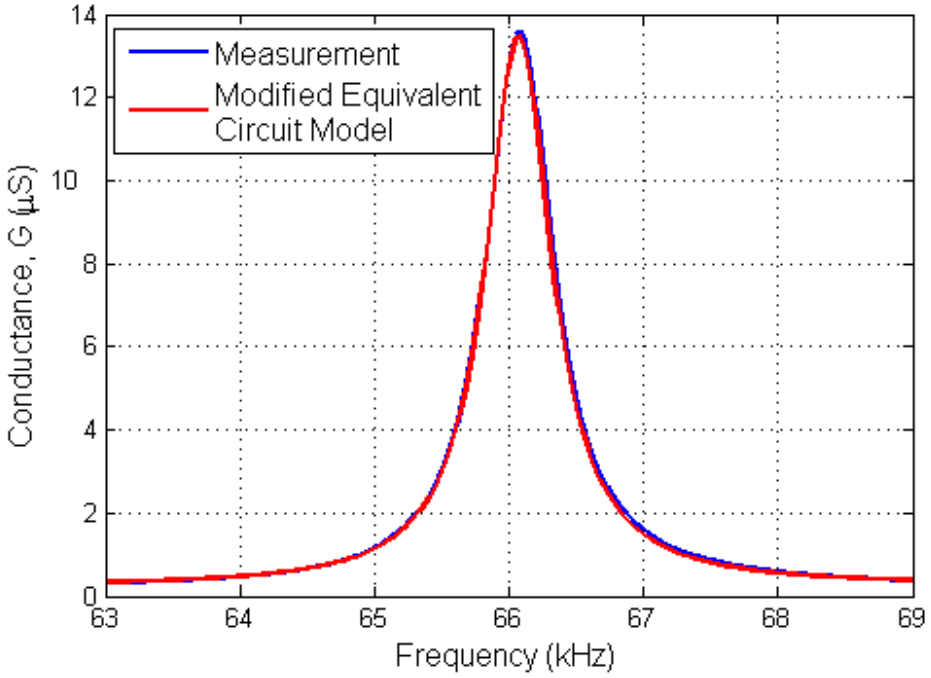

Figure A.8: Input electrical impedance of CMUT cell in set-III with a radius of 2.2 mm.

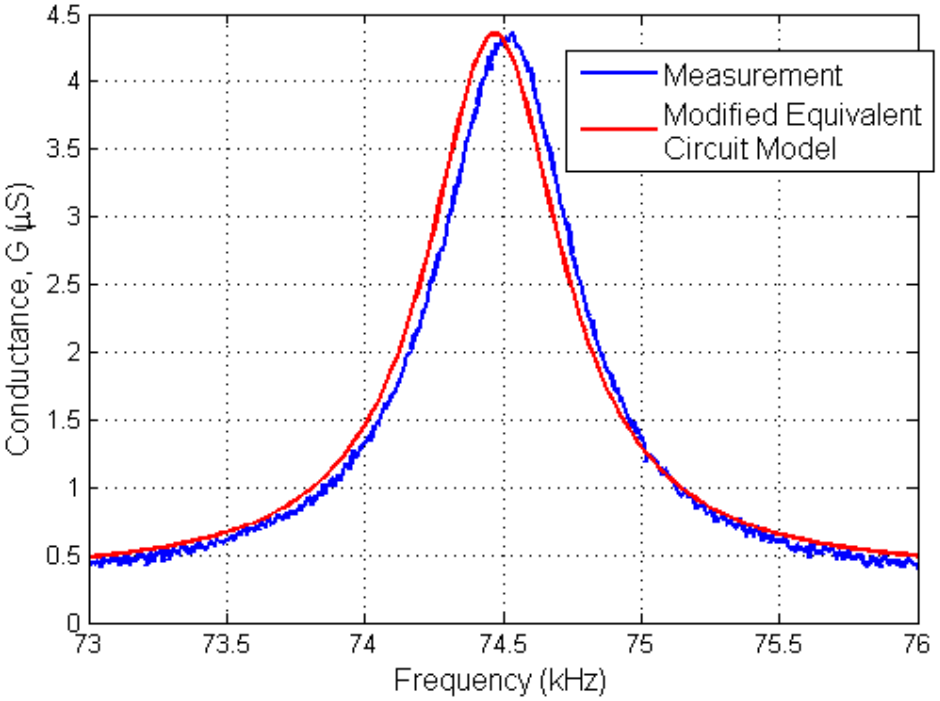

Figure A.9: Input electrical impedance of CMUT cell in set-IV with a radius of 2.0 mm.

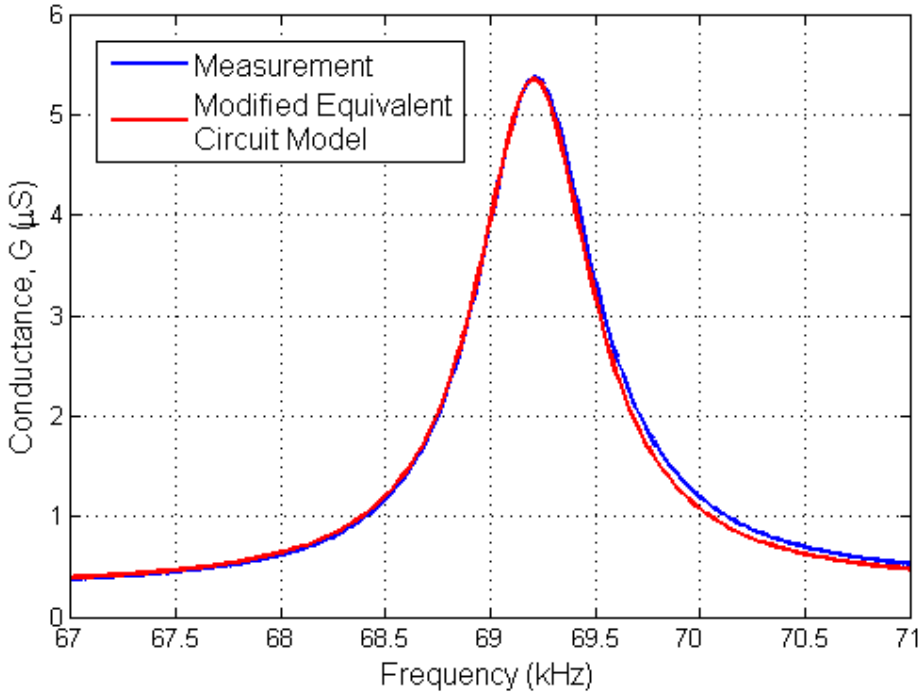

Figure A.10: Input electrical impedance of CMUT cell in set-IV with a radius of 2.1 mm.

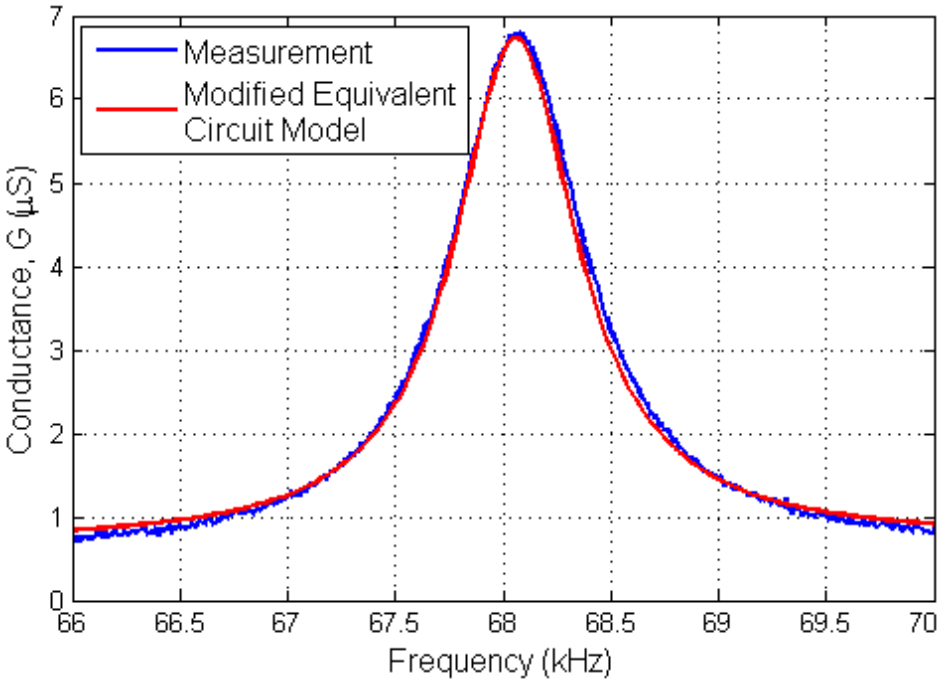

Figure A.11: Input electrical impedance of CMUT cell in set-IV with a radius of 2.15 mm.

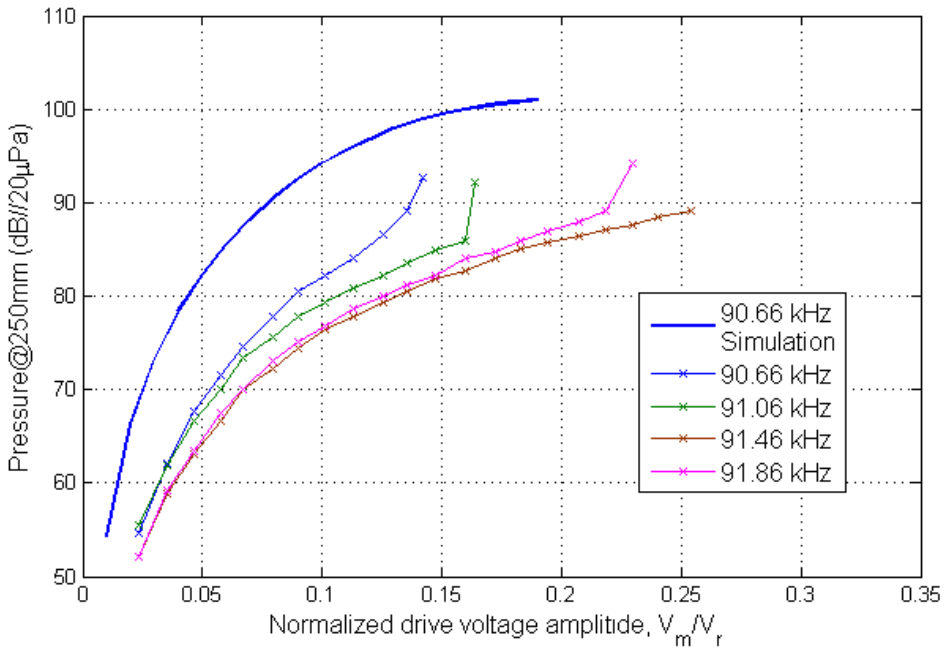

Figure A.12: Free field pressure measurement of CMUT cell in set-II with a radius of 1.8 mm.

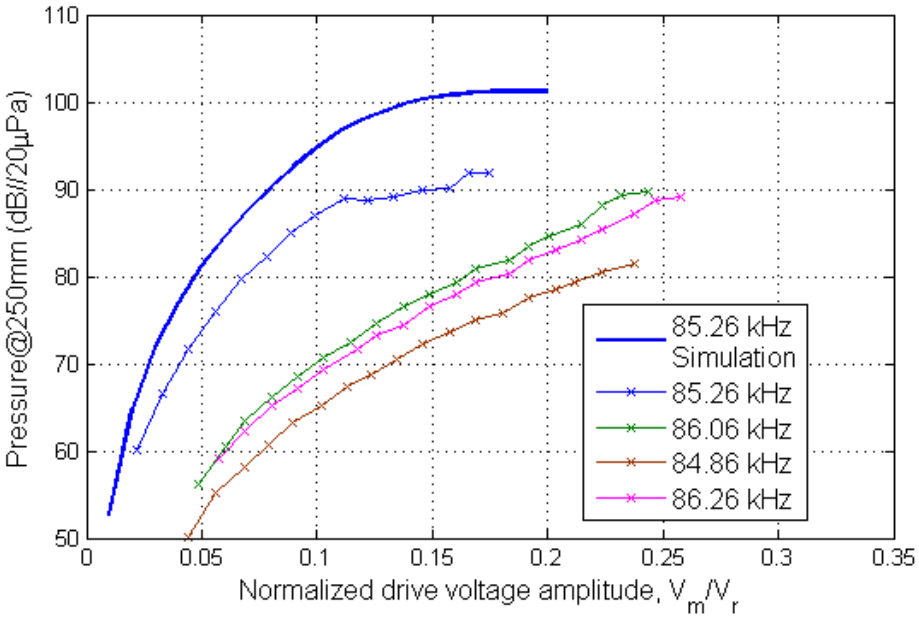

Figure A.13: Free field pressure measurement of CMUT cell in set-II with a radius of 1.85 mm.

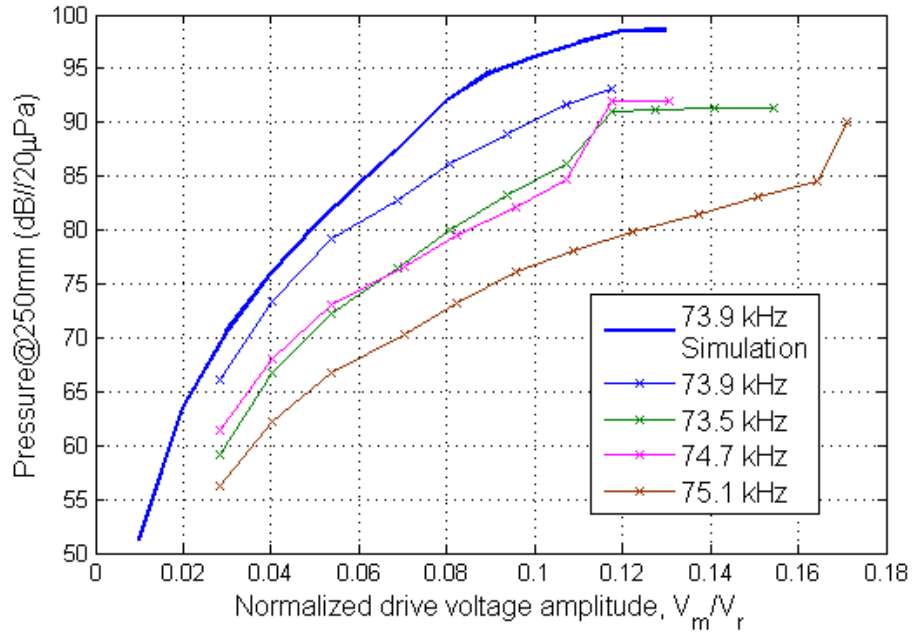

Figure A.14: Free field pressure measurement of CMUT cell in set-III with a radius of 2.0 mm.

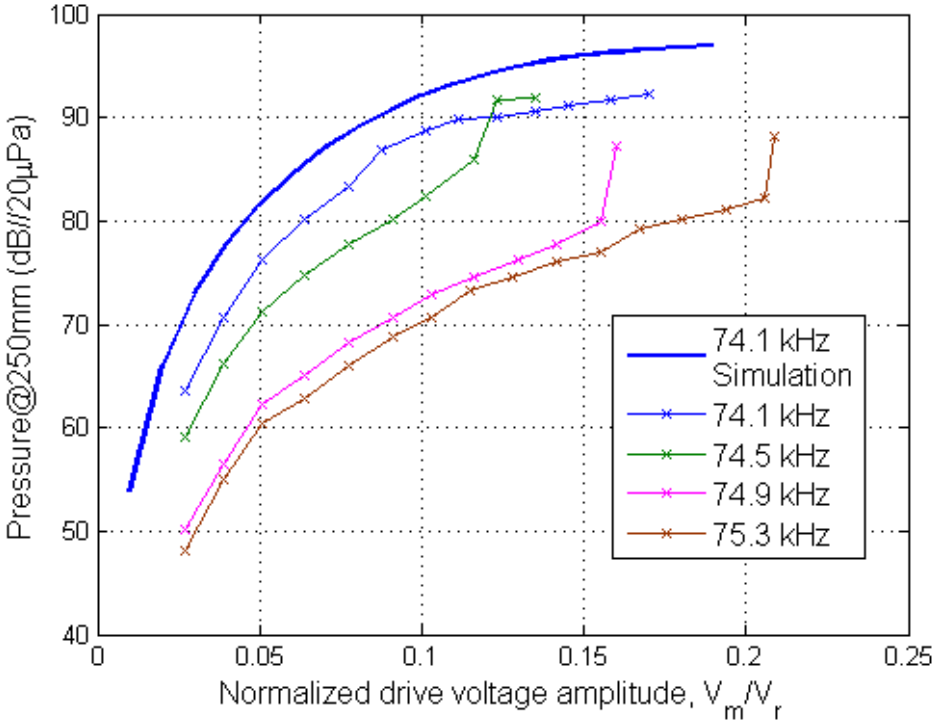

Figure A.15: Free field pressure measurement of CMUT cell in set-III with a radius of 2.05 mm.

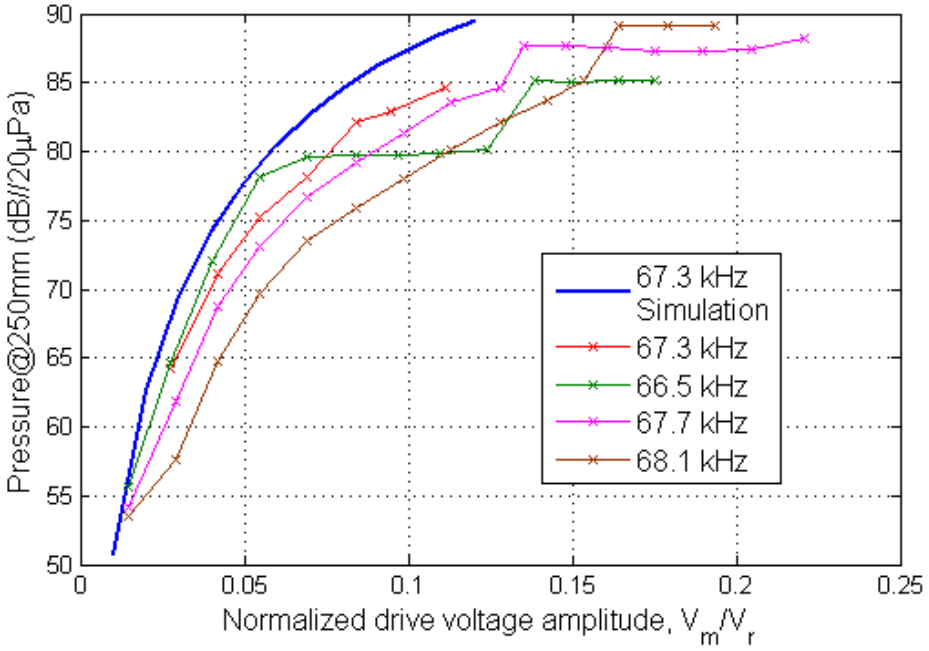

Figure A.16: Free field pressure measurement of CMUT cell in set-III with a radius of 2.15 mm.

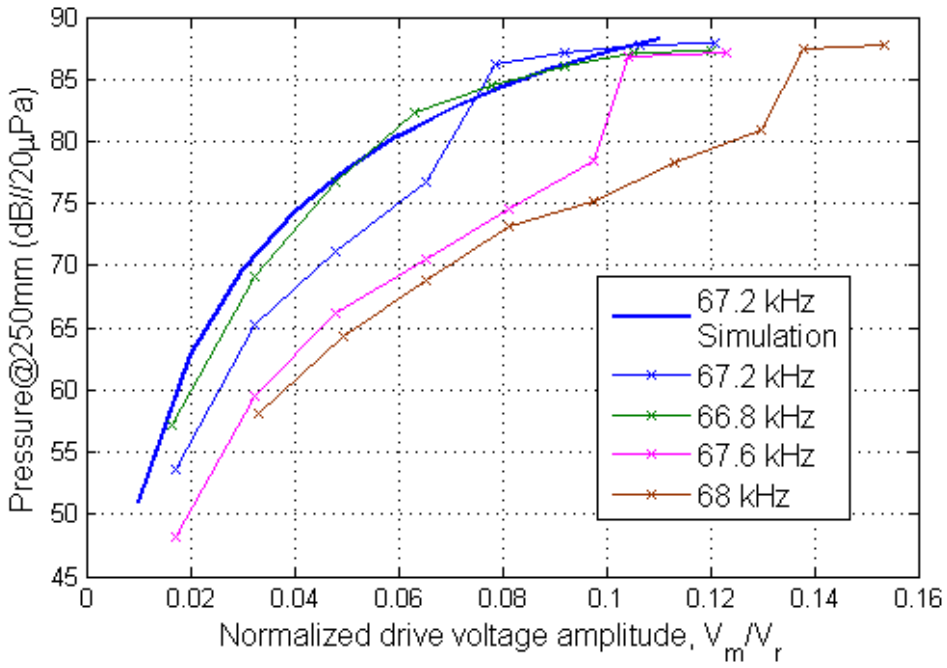

Figure A.17: Free field pressure measurement of CMUT cell in set-III with a radius of 2.2 mm.

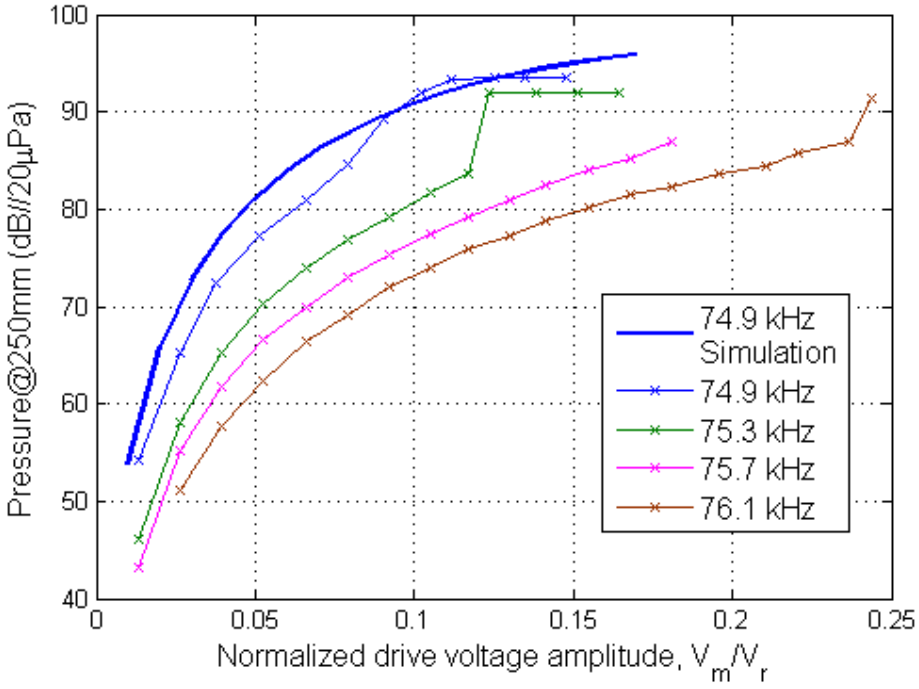

Figure A.18: Free field pressure measurement of CMUT cell in set-IV with a radius of 2.0 mm.

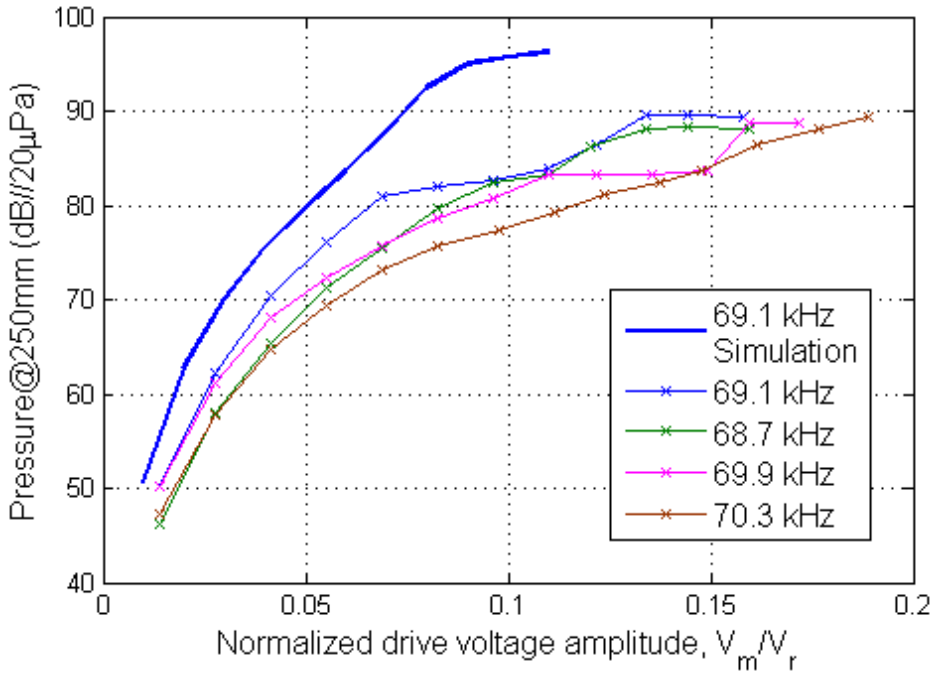

Figure A.19: Free field pressure measurement of CMUT cell in set-IV with a radius of 2.1 mm.

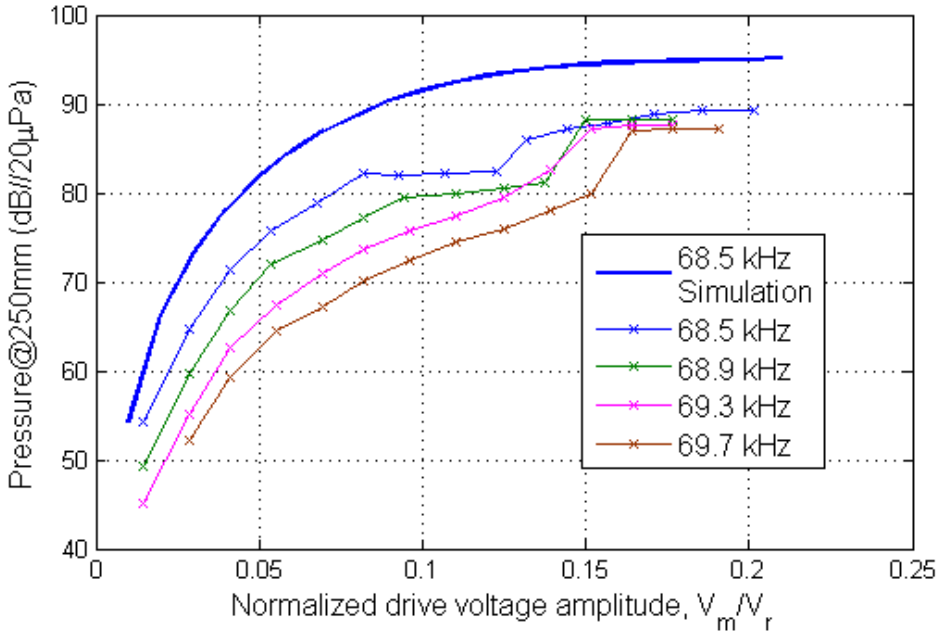

Figure A.20: Free field pressure measurement of CMUT cell in set-IV with a radius of 2.15 mm.

Bibliography

[1] S. Adler, P. Johnson, and I. O. Wygant, "Low frequency CMUT with vent holes," June 4 2013. US Patent 8,455,963.

[2] J. McIntosh, D. Hutchins, D. Billson, T. Robertson, R. Noble, and A. Jones, "The characterization of capacitive micromachined ultrasonic transducers in air," *Ultrasonics*, vol. 40, no. 1, pp. 477–483, 2002.

[3] W. Wright and S. McSweeney, "A tethered front-plate electrode cmut for broadband air-coupled ultrasound," in *Ultrasonics Symposium (IUS), 2013 IEEE International*, pp. 1716–1719, July 2013.

[4] D. Hutchins, D. Schindel, A. Bashford, and W. Wright, "Advances in ultrasonic electrostatic transduction," *Ultrasonics*, vol. 36, no. 1, pp. 1–6, 1998.

[5] C. Li, D. A. Hutchins, and R. J. Green, "Response of an ultrasonic communication channel in air," *IET communications*, vol. 6, no. 3, pp. 335–343, 2012.

[6] I. O. Wygant, M. Kupnik, J. C. Windsor, W. M. Wright, M. S. Wochner, G. G. Yaralioglu, M. F. Hamilton, and B. T. Khuri-Yakub, "50 khz capacitive micromachined ultrasonic transducers for generation of highly directional sound with parametric arrays," *Ultrasonics, Ferroelectrics and Frequency Control, IEEE Transactions on*, vol. 56, no. 1, pp. 193–203, 2009.

[7] C. Canali, G. De Cicco, B. Morten, M. Prudenziati, and A. Taroni, "A temperature compensated ultrasonic sensor operating in air for distance and proximity measurements," *Industrial Electronics, IEEE Transactions on*, no. 4, pp. 336–341, 1982.

[8] R. Hickling and S. P. Marin, "The use of ultrasonics for gauging and proximity sensing in air," *The Journal of the Acoustical Society of America*, vol. 79, no. 4, pp. 1151–1160, 1986.

[9] L. Mauritzson, J. Ilver, G. Benoni, K. Lindström, and S. Willner, "Two-dimensional airborne ultrasound real-time linear array scannerapplied to screening for scoliosis," *Ultrasound in medicine & biology*, vol. 17, no. 5, pp. 519–528, 1991.

[10] T. Tsujimura, T. Morimitsu, and T. Yabuta, "Shape-reconstruction system for three-dimensional objects using an ultrasonic distance sensor mounted on a manipulator," *Journal of dynamic systems, measurement, and control*, vol. 111, no. 2, pp. 180–186, 1989.

[11] K. K. Park and B. T. Khuri-Yakub, "3-d airborne ultrasound synthetic aperture imaging based on capacitive micromachined ultrasonic transducers," *Ultrasonics*, vol. 53, no. 7, pp. 1355–1362, 2013.

[12] K. Suzuki, K. Higuchi, and H. Tanigawa, "A silicon electrostatic ultrasonic transducer," *Ultrasonics, Ferroelectrics and Frequency Control, IEEE Transactions on*, vol. 36, no. 6, pp. 620–627, 1989.

[13] M. J. Anderson, J. A. Hill, C. M. Fortunko, N. S. Dogan, and R. D. Moore, "Broadband electrostatic transducers: Modeling and experiments," *The Journal of the Acoustical Society of America*, vol. 97, no. 1, pp. 262–272, 1995.

[14] H. Carr and C. Wykes, "Diagnostic measurements in capacitive transducers," *Ultrasonics*, vol. 31, no. 1, pp. 13–20, 1993.

[15] M. Oksanen, J. Vans, J. Hietanen, and J. Wu, "Quantitative theory for v-groove capacitive transmitting transducers," *Ultrasonics*, vol. 35, no. 3, pp. 205–211, 1997.

[16] M. I. Haller and B. T. Khuri-Yakub, "A surface micromachined electrostatic ultrasonic air transducer," *Ultrasonics, Ferroelectrics and Frequency Control, IEEE Transactions on*, vol. 43, no. 1, pp. 1–6, 1996.

[17] M. Kupnik, M.-C. Ho, S. Vaithilingam, and B. T. Khuri-Yakub, "CMUTs for air coupled ultrasound with improved bandwidth," in *Ultrasonics Symposium (IUS), 2011 IEEE International*, pp. 592–595, IEEE, 2011.

[18] B. Bayram, "Diamond-based capacitive micromachined ultrasonic transducers," *Diamond and Related Materials*, vol. 22, pp. 6–11, 2012.

[19] E. Ventsel and T. Krauthammer, *Thin plates and shells: theory: analysis, and applications*. CRC press, 2001.

[20] L. Landau and E. Lifshitz, *Mechanics*. Butterworth-Heinemann, Oxford, 1999.

[21] K. E. Petersen, "Silicon as a mechanical material," *Proceedings of the IEEE*, vol. 70, no. 5, pp. 420–457, 1982.

[22] M. Greenspan, "Piston radiator: Some extensions of the theory," *The Journal of the Acoustical Society of America*, vol. 65, no. 3, pp. 608–621, 1979.

[23] S. Timoshenko, S. Woinowsky-Krieger, and S. Woinowsky, *Theory of plates and shells*, vol. 2. McGraw-hill New York, 1959.

[24] H. Kagan Oguz, S. Olcum, M. N. Senlik, V. Tas, A. Atalar, and H. Koymen, "Nonlinear modeling of an immersed transmitting capacitive micromachined ultrasonic transducer for harmonic balance analysis," *Ultrasonics, Ferroelectrics and Frequency Control, IEEE Transactions on*, vol. 57, no. 2, pp. 438–447, 2010.

[25] C. Wallace, "Radiation resistance of a baffled beam," *The Journal of the Acoustical Society of America*, vol. 51, no. 3B, pp. 936–945, 1972.

[26] A. Unlugedik, A. Atalar, and H. Koymen, "Designing an efficient wide bandwidth single cell CMUT for airborne applications using nonlinear effects," in *Ultrasonics Symposium (IUS), 2013 IEEE International*, pp. 1416–1419, IEEE, July 2013.

[27] M. Kupnik, I. O. Wygant, and B. T. Khuri-Yakub, "Finite element analysis of stress stiffening effects in CMUTs," in *Ultrasonics Symposium, 2008. IUS 2008. IEEE*, pp. 487–490, IEEE, 2008.

[28] A. A. Batista, F. Oliveira, and H. Nazareno, "Duffing oscillators: Control and memory effects," *Physical Review E*, vol. 77, no. 6, p. 066216, 2008.

[29] V. Kaajakari, T. Mattila, A. Oja, and H. Seppa, "Nonlinear limits for single-crystal silicon microresonators," *Microelectromechanical Systems, Journal of*, vol. 13, no. 5, pp. 715–724, 2004.

[30] P. Holmes and D. Rand, "The bifurcations of duffing's equation: An application of catastrophe theory," *Journal of Sound and Vibration*, vol. 44, no. 2, pp. 237–253, 1976.

[31] S. Machida, S. Migitaka, H. Tanaka, K. Hashiba, H. Enomoto, Y. Tadaki, and T. Kobayashi, "Analysis of the charging problem in capacitive micromachined ultrasonic transducers," in *Ultrasonics Symposium, 2008. IUS 2008. IEEE*, pp. 383–385, IEEE, 2008.

[32] K. Midtbo and A. Ronnekleiv, "Analysis of charge effects in high frequency CMUTs," in *Ultrasonics Symposium, 2008. IUS 2008. IEEE*, pp. 379–382, IEEE, 2008.

[33] S. Olcum, F. Y. Yamaner, A. Bozkurt, and A. Atalar, "Deep-collapse operation of capacitive micromachined ultrasonic transducers," *Ultrasonics, Ferroelectrics and Frequency Control, IEEE Transactions on*, vol. 58, no. 11, pp. 2475–2483, 2011.

[34] P. Zhang, G. Fitzpatrick, W. Moussa, and R. J. Zemp, "CMUTs with improved electrical safety & minimal dielectric surface charging," in *Ultrasonics Symposium (IUS), 2010 IEEE*, pp. 1881–1885, IEEE, 2010.

[35] F. Y. Yamaner, S. Olcum, H. K. Oguz, A. Bozkurt, H. Koymen, and A. Atalar, "High-power CMUTs: design and experimental verification," *Ultrasonics, Ferroelectrics and Frequency Control, IEEE Transactions on*, vol. 59, no. 6, pp. 1276–1284, 2012.

[36] J. Zahorian, M. Hochman, S. Satir, and F. L. Degertekin, "Bias optimization of dual ring CMUT arrays for forward looking ivus applications," in *Ultrasonics Symposium (IUS), 2010 IEEE*, pp. 447–450, IEEE, 2010.

[37] Bruel and Kjaer, *Condenser Microphones and micrphone preamplifiers for acoustic measurement*. Data Handbook, 1982.

[38] G. Kaye and T. Laby, *Tables of physical and chemical constants*. Longman, 1995.

[39] H. Oguz, A. Atalar, *et al.*, "Equivalent circuit-based analysis of CMUT cell dynamics in arrays," *Ultrasonics, Ferroelectrics and Frequency Control, IEEE Transactions on*, vol. 60, no. 5, pp. 1016–1024, 2013.

[40] E. Aydogdu, A. Ozgurluk, H. Oguz, A. Atalar, and H. Koymen, "Lumped element model of single cmut in collapsed mode," in *Ultrasonics Symposium (IUS), 2013 IEEE International*, pp. 283–286, July 2013.